Marine and Petroleum Geology 140 (2022) 105662

Contents lists available at ScienceDirect

Marine and Petroleum Geology

journal homepage: www.elsevier.com/locate/marpetgeo

Application of μXRF analysis on the Upper Cretaceous Mancos Shale: A comparison with ICP-OES/MS

Jeremy J. Gabriel [a,*], Eduard G. Reinhardt [a], Xueke Chang [b], Janok P. Bhattacharya [a]

[a] School of Earth, Environment & Society, McMaster University, 1280 Main St W, Hamilton, Ontcario, L8S 4K1, Canada
[b] Department of Earth Sciences, University of Western Ontario, 1151 Richmond St, London, Ontario, N6A 3K7, Canada

ARTICLE INFO

Keywords:
Chemofacies
Mudstone
μXRF core Scanning
Mancos shale
Itrax

ABSTRACT

This study investigates the elemental signature of fine-grained sedimentary rock (mudstone) obtained using energy-dispersive micro-X-ray fluorescence (μXRF). A short section (28.5 cm) of Upper Cretaceous Mancos Shale was analysed with an Itrax μXRF core scanner at 0.2 mm intervals for comparison to elemental and petrographic composition. Fifteen subsamples were collected at 2 cm intervals for ICP-OES/MS analysis to obtain absolute concentrations of elements and oxides, and thin sections were used for petrographic and microfacies analysis. The data obtained from the Itrax core scanner show a high level of reproducibility between separate scans and moderate to strong Spearman-Rho correlation ($R^2 > 0.6$) to ICP-derived concentrations for several oxides: Fe_2O_3, SiO_2, Al_2O_3, K_2O, TiO_2, and MnO. Common elemental ratios used in palaeoenvironmental studies (e.g., Zr/Rb, Ca/Ti, Mn/Ti) also showed good correlation to ICP-derived data when the trends were compared. The elemental signature obtained from the Itrax also showed good relationships to the petrography and lithology, with the Si/Ti ratio accurately identifying quartz-rich layers, and the Ca/Ti and Mn/Ti ratios corresponding to increased carbonate content, which are of importance in the planning of hydraulic fracturing for unconventional resources. At core scale, the elemental trends in Zr/Rb, Ti, and Si were useful for detecting short-term, rapid patterns of sedimentary events, likely resulting from storm activity (e.g., tempestites, wave-enhanced sediment gravity flows). The high-sampling resolution data from μXRF core scanners can provide advantages over traditional geochemical techniques since data aliasing is minimized. Analysing these elements and ratios in longer core sections from the Mancos Shale may serve as a proxy for determining high-frequency climatic changes in the Cretaceous Interior Seaway and allow for improved correlations of intra- and inter-basinal events in other Cretaceous basins.

1. Introduction

Fine-grained siliciclastic rocks (<63 μm) comprise approximately half to two-thirds of the global sedimentary record (Dypvik and Harris, 2001; Boggs and Boggs, 2009) and although traditionally they have been viewed as indicating deposition from suspension settling in low-energy environments, recent research (e.g., Bhattacharya and MacEachern, 2009; Macquaker et al., 2010; Plint et al., 2012; Plint, 2014; Wilson and Schieber, 2014; Schieber, 2016) has shown that mud can also be deposited in hemipelagic environments that are subject to significant wave, tidal, and bottom-current energy, and thus often contain similar bedforms to those found in shallower environments (e.g., ripples, cross-lamination, grading). However, the textural and lithological changes in these sediments can be subtle and may not be visible in slabbed rock core without petrographic analysis, making the study of mudstones significantly more complex than sandstones (Dypvik and Harris, 2001).

Chemostratigraphy of fine-grained rock and sediment cores based on elemental and isotopic composition has been used to effectively show changes in precipitation patterns (e.g., Haug et al., 2003; Zarriess and Mackensen, 2010), provenance and sediment transport processes (e.g., Chen et al., 2013; Ben-Awuah et al., 2017), and bottom-water redox conditions (e.g., Algeo and Rowe, 2012; Baioumy and Lehmann, 2017) in both modern and ancient systems; a search of the literature showed over 1500 publications relating to chemostratigraphy or chemofacies since 2000 (Web of Science, Clarivate Analytics). Two common techniques for elemental and isotopic analysis are inductively-coupled plasma optical emission spectrometry/mass spectrometry

* Corresponding author.
E-mail address: gabriejj@mcmaster.ca (J.J. Gabriel).

https://doi.org/10.1016/j.marpetgeo.2022.105662
Received 26 October 2021; Received in revised form 14 March 2022; Accepted 19 March 2022
Available online 6 April 2022

(ICP-OES/MS), and wavelength-dispersive X-ray fluorescence (WD-XRF), which can detect 55 and 42 elements, respectively, with an analytical precision as low as parts per million or billion (ppm/ppb) for some elements and oxides. This provides at least 42 highly accurate variables for use in chemostratigraphic correlations and when elemental ratios (e.g., Ti/Al, Zr/Rb, Ca/Fe) are used, the number of variables can exceed 250 (Craigie, 2018). However, these methods are destructive and can be very intensive in terms of time (subsampling, sample preparation, pre-treatment) and cost, so down-core sampling resolution is often on the order of 1 sample per metre. Subsamples are collected, ground, and homogenised into roughly 1–2g of fine (<10 μm) powder, which is then liquefied, for ICP-OES/MS analysis (Craigie, 2018), or fused and pressed into a lithium-borate pellet, for WD-XRF analysis (Weltje and Tjallingii, 2008; Gregory et al., 2019). The pre-treatment method chosen (e.g., acid digestion, alkali fusion) can result in different detection limits and accuracy of certain elements so the desired variables should be considered prior to analysis. One centimetre sampling and analysis of a metre-long core could take a couple weeks (Croudace et al., 2006) and cost thousands of dollars, and since the methods are destructive, replicate analyses would require the collection of more material, which may have a different elemental composition due to vertical and lateral heterogeneities.

Recently (~20 years), technological advancement of core scanners using energy-dispersive XRF (ED-XRF), such as the Itrax Core Scanner (Cox Systems, Sweden), has allowed for a much higher sampling resolution (100 μm) from marine and lacustrine sediment cores (Rothwell and Rack, 2006; Rothwell and Croudace, 2015; Löwemark et al., 2019); herein, this method is referred to as μXRF. These core scanners allow for rapid and non-destructive analysis of elemental composition from Al (Z = 13) to U (Z = 92) by recording the spectrum of energy intensities, in keV, from emitted photons. Energy-dispersive XRF does not have the elemental precision of WD-XRF but it can rapidly collect data on more variables simultaneously than WD-XRF, which requires a diffraction crystal that is tuned to permit transmission of a specific wavelength (element) of interest. The core requires minimal preparation, aside from ensuring a flat, even surface and there are no pre-treatments necessary since the sample or split core is placed into the core scanner whole for analysis (Löwemark et al., 2019). The Itrax is equipped with a 3 kW X-ray generating tube, typically of either Cr or Mo, and can be operated up to 60 kV and 50 mA, although 30 kV and 30 mA is suitable for detecting most elements (Croudace et al., 2006); other user-defined options include measurement interval and exposure time (from 1 s to 1 min). Split cores up to 1.8 m in length can be analysed in a single, automated scan, which could be completed in less than 2 h (1.8 m at 1 cm interval and 30 s exposure time) and provide hundreds to thousands of sampling intervals. As the data acquired by μXRF core scanners are in total counts of emitted photons, the final result will not only be a function of the presence and abundance of the various elements within the core, but also a function of the exposure time and power of the incident beam. Furthermore, since a discrete sample is not homogenised prior to analysis, the interval can be heterogeneous in terms of grain size, pore space, organic matter, and water content (so-called *matrix effects*; Croudace et al., 2006; Tjallingii et al., 2007). These matrix effects can lead to increased scattering, which can influence the final spectra, with the effects being more pronounced with lighter elements that eject lower energy photons (Tjallingii et al., 2007). However, several studies have shown that calibration of elemental intensities obtained from ED-XRF to absolute concentrations is possible through statistical analysis and comparison to values obtained using ICP-OES/MS and WD-XRF (e.g., Weltje and Tjallingii, 2008; Rowe et al., 2012; Weltje et al., 2015; Al Maliki et al., 2017; Arenas-Islas et al., 2019; Gregory et al., 2019). Weltje et al. (2015) showed that the most accurate method was a multivariate log-ratio calibration (MLC), in which the ratios of elemental intensities measured from μXRF are compared with concentrations measured using ICP-OES/MS. While this method provides more accurate estimates of absolute element concentrations from their measured intensities, it does increase time and cost of the analysis (Gregory et al., 2019). A univariate log-ratio calibration (ULC), which relates "relative" element concentration (W) to the elemental intensity (I), does not require calibration against data from other methods and can be used to adequately describe the system through the linear relationship:

$$ln\left(\frac{W_{ij}}{W_{iD}}\right) = \alpha_{jD} ln\left(\frac{I_{ij}}{I_{iD}}\right) + \beta_{jD} \quad (1)$$

where j and D represent the two different elements being measured at interval i and α_{jD} and β_{jD} account for the matrix effect and detection efficiency, respectively. It is considered a relative concentration since all the elements measured are constrained to unity, despite the fact that not every element (i.e., $Z < 13$ and $Z > 92$) can be detected. Gregory et al. (2019) found that normalizing elements to the X-ray scatter ratio (incoherent:coherent) produced statistically significant results and this divisor is often used in palaeoenvironmental studies to account for water content (e.g., Boyle et al., 2015) and organic matter (e.g., Brown et al., 2007).

Micro-XRF core scanners have been used extensively in research on soft sediment cores (see Croudace and Rothwell, 2015 and Rothwell, 2006 for a comprehensive review) but more recently they have also been applied to coal seams (Kelloway et al., 2014; Ward et al., 2018), speleothems (Scroxton et al., 2018), tephras (Peti et al., 2019), and glass samples (Ernst et al., 2014). Their use on rock cores, however, is lacking (e.g., Ma et al., 2014; Beil et al., 2018). Micro-XRF is an optimal method for chemofacies analysis of rock cores because the cut surface of the core is smooth and flat and the matrix effects are minimized, especially with fine-grained rocks like siltstone and shale.

This study focuses on a short section (28.5 cm; herein referred to as the 'Cheese Slab') of the Blue Gate Formation of the Mancos Shale, a muddy shelf deposit from the Upper Cretaceous Western Interior Seaway of North America. The Cheese Slab was collected from a proprietary quarry in the Uinta Basin, Utah, by TerraTek/Schlumberger and provided to McMaster University by the New Mexico Institute of Mining and Technology. The goal of this study is to examine trends in the μXRF-derived elemental intensities and how they correspond to the mineral and elemental composition based on petrographic and ICP-OES/MS analysis, respectively. The μXRF data will also be compared to the macro- and microscale lithology to demonstrate how it can be used to identify and refine lithofacies for eventual application to longer successions of Mancos Shale. Finally, this study will demonstrate the potential of μXRF-derived chemofacies to identify characteristics such as provenance (marine vs. terrestrial), flooding surfaces, and geomechanical properties that are important to the exploration and extraction of hydrocarbons.

1.1. Geologic background

The Mancos Shale was deposited into the Western Interior Seaway (WIS) of North America, which covered the central part of the continent during the Upper Cretaceous (Cenomanian - mid-Campanian; Fig. 1). Subduction of the ancient Farallon Plate during westward migration of the North American tectonic plate caused building and uplift of the Sevier orogeny on the western margin of the North American plate resulting in the formation of an asymmetric foreland basin (Armstrong, 1968; Miall et al., 2008; El-Attar and Pranter, 2016; Lowery et al., 2018). Several marine transgressions occurred in the WIS throughout the Cretaceous, but a trangression during the Cenomanian and Turonian brought sea level to almost 300 m higher than present (McDonough and Cross, 1991; Miall et al., 2008; Haq and Huber, 2017). At this time, the WIS spanned it's maximum extent, connecting the northern Boreal (Arctic) Ocean with the southern Tethys (Gulf of Mexico). During this highstand several deltaic complexes, such as the Ferron, Frontier, and Gallup, were deposited into the WIS, as sediments were eroded from the

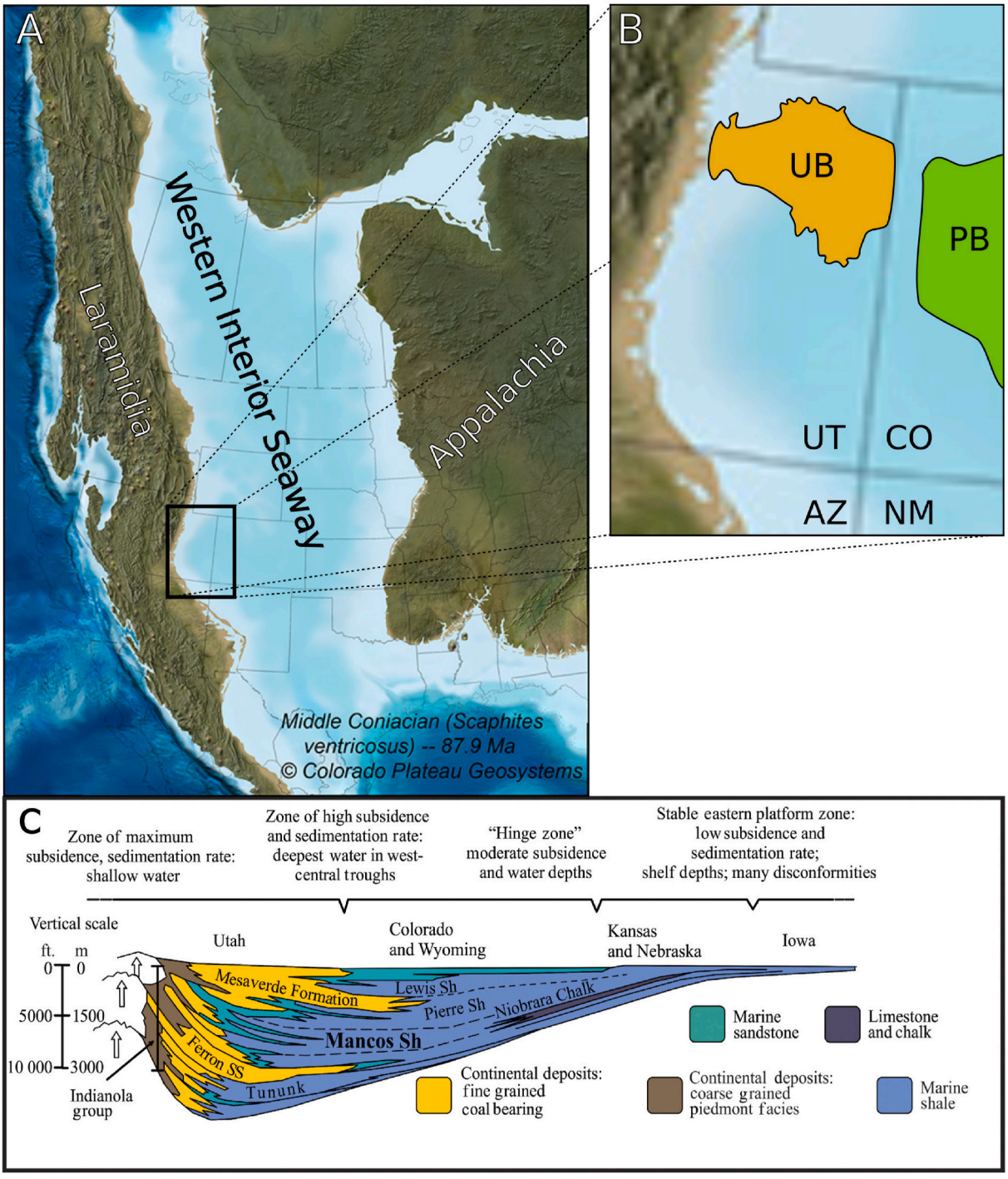

Fig. 1. A) Reconstruction of North America during the Upper Cretaceous (mid-Coniacian, ~87.9 Ma; basemap from Colorado Plateau Geosystems www.deeptimemaps.com). B) Close up of the Uinta Basin (UB, location from Birgenheier et al., 2017) and Piceance Basin (PB, location from Hawkins et al., 2016); the two basins are separated by the Douglas Arch. C) Generalized west-east transect of the Uinta basin from Birgenheier et al. (2017) (originally in Armstrong, 1968).

nearby Sevier orogenic belt and transported eastward (Armstrong, 1968; Bhattacharya and MacEachern, 2009; Lin et al., 2019), and the Mancos Shale represents the distal extent of those complexes. During the Laramide orogeny of the late Upper Cretaceous and early Palaeogene, the basin was segmented into several sub-basins such as the Uinta (Utah), Piceance (central-western Colorado), and the San Juan and Zuni (north-western New Mexico), which preserved the Upper Cretaceous marine sequences (Ridgley et al., 2013; Broadhead, 2015; Hawkins et al., 2016). Due to the exceptional outcrop exposure and preservation, these fluvio-deltaic complexes have been extensively studied in terms of their facies architecture and sequence stratigraphy (e.g., Zhu et al., 2012; Li and Bhattacharya, 2013; Ahmed et al., 2014; Eldrett et al., 2015; Wu et al., 2015; Li and Schieber, 2018; Lin et al., 2019) with other studies looking into isotope chemostratigraphy (e.g., Joo and Sageman, 2014), microfossil assemblages (e.g., Lowery et al., 2018; Turkistani, 2020) and palynology (e.g., Akyuz et al., 2016). The combined results of these studies indicate that the early-mid Upper Cretaceous climate of the southern WIS was an ever-wet, sub-tropical to tropical environment. In the Uinta basin, the Mancos Shale is over 1200 m thick with a high detrital quartz and clay content relative to carbonate sediment

(Birgenheier et al., 2017). It is separated into two members that span the mid-Turonian to late-Campanian (~92-79 Ma): the lower Tununk shale, which unconformably overlies the paralic Dakota Formation, and the upper, more extensive Blue Gate shale; the two units are separated by an organic-rich heterolith called the Juana Lopez Member (Molenaar and Cobban, 1991). Fine-grained sediment deposition in more distal marine environments (distal prodelta and mudbelt) has been a common focus of research in recent years (e.g., Bhattacharya and MacEachern, 2009; Macquaker et al., 2010; Plint et al., 2012; Plint, 2014; Wilson and Schieber, 2014; Schieber, 2016), as mudstones typically contain a more continuous record than near-shore deposits, which are more prone to periods of erosion and gaps in deposition (Bhattacharya et al., 2019). Birgenheier et al. (2017) developed a detailed record of the lower Blue Gate member based on lithology, stratigraphy and geochemistry, obtained using a handheld ED-XRF unit at 0.3–0.9 m intervals. They characterised ten facies based on grain size, mineralogic composition, and sedimentary structures, such as lamination and ripple style, that were deposited in three different marine settings: prodelta, mudbelt, and sediment-starved shelf (Fig. 2). The prodelta, which is closest to the shoreline, contains interlaminated siltstone to very fine sandstone, with a medium to high detrital quartz content, and is dominated by river-fed hyperpycnal flow. The hyperpycnites observed were characterised by normal grading and basal scour (i.e. asymmetrical), with evidence of dewatering due to a high rate of sediment input. Moving further into the basin, the mudbelt spans storm-wave base and was divided into six facies. The upper two facies were interpreted to have been deposited above storm-wave base, due to the very high detrital quartz content and intense reworking from storm waves and bioturbation. The other four facies of the mudbelt were deposited below storm-wave base and typically showed the distal expressions of wave-enhanced sediment gravity flows (WESGFs; Macquaker et al., 2010) that were initiated above storm-wave base but flowed downslope. These facies had increasing preservation of lamination and ripples, higher clay content (mainly illite and kaolinite), and low to moderate bioturbation (BI = 2–3), although in some areas it was higher (BI = 5) (Birgenheier et al., 2017). Finally, the sediment-starved shelf contained moderate to high clay and calcite content (values not seen in the other facies) and showed only faint laminations and low bioturbation levels due to suboxic conditions. This area was mainly influenced by shelfal currents in the proximal shelf and suspension settling more distally (Birgenheier et al., 2017).

Generally, the three processes responsible for moving and depositing muddy sediments across epicontinental seas are: river-fed *hypo*pycnal plumes; river-fed *hyper*pycnal flows; and submarine ignitive gravity flows, which can be aided by wave or bottom currents (Schieber, 2016). Hypopycnal plumes typically come from large, continent-scale rivers (e.g. Mississippi, Amazon), which do not often have the sediment concentration to become hyperpycnal, and can travel long distances (100 s km) from the river mouth by longshore currents. Hyperpycnal flows are more commonly associated with small, 'dirty' rivers, which were common on the western shore of the WIS. These 'dirty' rivers were susceptible to periods of intense flooding and sediment overload that produced sufficiently dense plumes that would sink and move along the seabed. Typically, a hyperpycnite will display a symmetrical grain size profile, with a basal inversely-graded unit overlain by a normally-graded unit as a result of changing flow velocities as the flood waxes and wanes. However, erosion of sediments during maximum flow or subsequent wave and current reworking may lead to asymmetric deposits (Schieber, 2016). Hyperpycnal flows require bottom slopes of $> 0.7^{\circ}$ to maintain autosuspension and are thus typically confined to within a few tens of kilometres of the river mouth, although the distance can be greater during periods of more intense fluvial weathering and mud generation (Bhattacharya and MacEachern, 2009). In more distal environments, bottom currents and wave action act together to suspend fine-grained sediments in a fluid mud, which can move down slopes with lower gradients (~0.03°) and tends to form normally graded thin beds with sharp, basal contacts. These deposits can be resuspended and moved several times and therefore can reach 100 s km from the shoreline. All three of these mechanisms can produce a similar succession in the rock record, thus differentiating between them based on lithology and sedimentary structures can be difficult (Schieber, 2016).

2. Methods

The *Cheese Slab* is a highly interbedded very fine sandstone to mudstone sequence with approximately 240 individual laminae (Fig. 3); grain sizes were estimated by microscope analysis of thin sections. Since accurate determination of grain size (i.e., silt vs. clay) in the darker, finer-grained lamina was not possible, herein we use the term *mudstone* to distinguish these from the lighter, coarser-grained sandstone laminae. A 6 cm wide and 2 cm thick piece was slabbed using a water-tile saw and adhered to a clear acrylic sheet using double-sided tape to allow for consistent positioning through the various analyses. Prior to being cut, the piece was vacuum-infused with an epoxy to prevent the fine-grained shale from being pulverized; this epoxy can be seen filling in the large

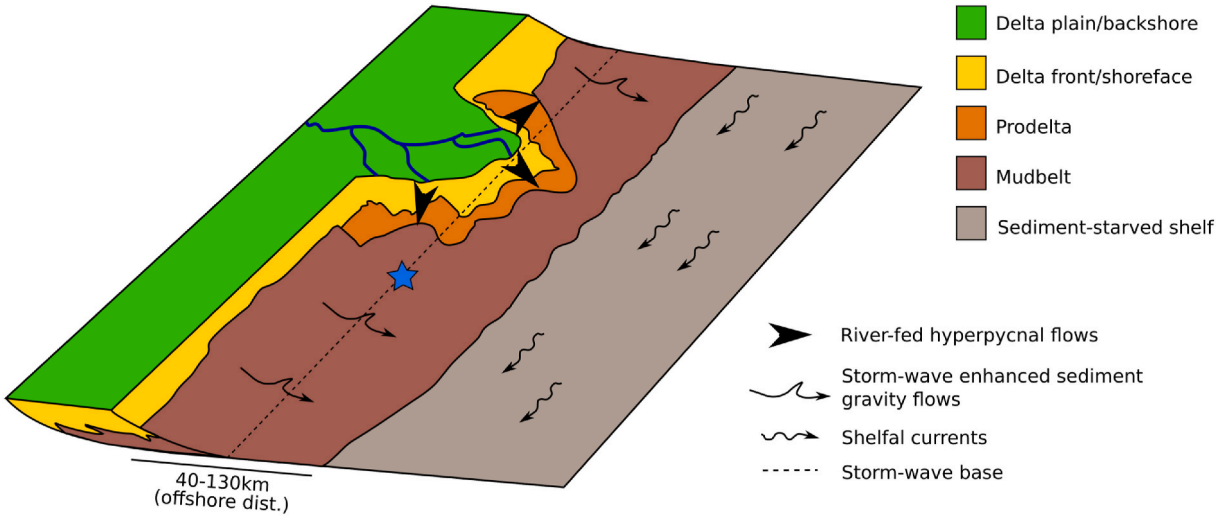

Fig. 2. Depositional environments and their relationship to shoreline and deltaic tributaries. Adapted from Birgenheier et al. (2017); after Bhattacharya (2010). Blue star demarcates approximate core location (see subsection 3.4 and subsection 4.2). (For interpretation of the references to colour in this figure legend, the reader is referred to the Web version of this article.)

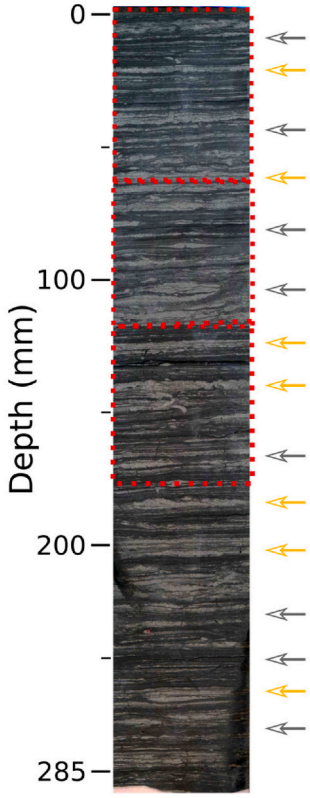

Fig. 3. The core section showing location of thin sections (dotted red boxes) and ICP-OES/MS samples (grey arrows are from a mudstone interval, yellow from sandstone). (For interpretation of the references to colour in this figure legend, the reader is referred to the Web version of this article.)

fracture at ~130 mm. Lithofacies were established by millimetre-scale analysis of the laminae to measure characteristics such as lamina thickness, relative grain size, presence/preservation of sedimentary structures, and bioturbation.

Three large-sized (5 × 7 cm) thin sections were made by Wagner Petrographic, Utah, USA from the opposing face of the scanned surface for petrographic analysis (A - top, B - middle, C - bottom). The samples were infused with a rose dye to accentuate microfractures and structures, ground to 25 μm, and polished (i.e., no slide cover). Each slide was digitally scanned with an Epson V850 Pro photo slide scanner (48-bit colour, 4800 dpi) in both plane-polarized (PPL) and cross-polarized (XPL) light to see the overall sedimentary structures and then analysed with a Leica petrographic microscope to determine the mineral composition. The remaining material from the thin section production was also analysed with the Itrax (30 kV, 33 mA, 200 μm, 15 s) to allow for precise alignment of the μXRF data to the structures and mineral content.

2.1. Itrax μXRF

Elemental intensities were obtained from five separate analytical runs using an Itrax μXRF Core Scanner (Cox Analytical Systems, Mölndal, Sweden) at the McMaster University Core Scanning Laboratory (MUCS-Lab): scans 1–4 were performed down the centre at 0.5 mm resolution (n = 571 observations), while scan 5 went down the right side at 0.2 mm resolution (n = 1425 observations) for comparison to the ICP-OES/MS data (Table 1). The X-ray beam is 8 mm long, perpendicular to the longitudinal axis, and 0.1 mm wide (0.8 mm^2; Kelloway et al., 2014), with a penetration depth on the order of 1 mm, though penetration may be even less in denser material like siltstone and shale. The raw energy spectra of each analytical scan were batch evaluated in QSpec software

Table 1
Itrax run parameters.

Run	Tube Parameters				
	kV	mA	Exposure time (sec)	Interval (mm)	Position
1–4	30	33	15	0.5	Centre
5	30	33	15	0.2	Right

(Cox Analytics) and an additional calibration was performed on scan 5 using the Cody Shale (USGS rock standard Sco-1), which is an Upper Cretaceous formation from the Powder River Basin, Wyoming, USA (Hubert et al., 1972). The Cody calibration converts the elemental counts to major oxide (SiO_2, Al_2O_3, TiO_2, Fe_2O_3, K_2O, CaO, and MnO) concentrations in weight percent and the remaining elements in ppm. In addition to this calibration, the data were transformed using the ULC with the incoherent:coherent scatter ratio (ln ([Element]/ICR)).Counts per second (ln ([Element]/cps)), and a conservative element (ln ([Element]/[Si])) used as divisors to determine the impact on correlation between μXRF elemental intensities and ICP-OES/MS elemental concentrations (Cf. Gregory et al., 2019).

2.2. ICP-OES/MS

Fifteen subsamples (~0.2 g each), 8 mudstone and 7 sandstone (based on colour), were collected at roughly 2 cm intervals for analysis using inductively-coupled plasma techniques (ICP-OES/MS; see Fig. 3). For brevity, we will simply use ICP to refer to these methods collectively. A rotary drill (Foredom TX Series) with a diamond-encrusted carbide milling tip was used to collect about 0.2 g of material from individual laminae and pulverize the material into a fine powder (<40 μm). Each sample had a vertical width and penetration depth of 2–3 mm, while the horizontal length varied between 10 and 20 mm, which is a total sample footprint of ~40–180 mm^3. Samples were digested and analysed by Activation Laboratories Ltd in Ancaster, Ontario, Canada using a lithium metaborate/tetraborate fusion technique and analysed by ICP for major and trace element concentrations. Oxide results were presented for comparison with the Cody-calibrated μXRF data. When comparing the values between the two techniques, we used the Spearman-Rho correlation since it is more robust against outliers and the μXRF data are rarely normally-distributed, which is a requirement when using the Pearson correlation coefficient (Schober et al., 2018). In this paper, we have followed the terminology of Schober et al. (2018) when referring to the 'strength' of correlation, such that values >0.90 are considered 'very strong', 0.70–0.89 is considered 'strong', 0.40–0.69 is 'moderate', 0.1–0.39 is 'weak', and <0.1 is 'negligible', though we recognise that these specific cutoff values and descriptors are somewhat arbitrary (as discussed by Schober et al., 2018).

3. Results

3.1. Itrax reproducibility

Spectra from each sample interval record the total counts (cts) of energy intensities, which are compared to the 'expected' intensity curve based on the user-defined elements using a least mean-square error (MSE) method. The average individual MSE for all intervals in the four runs was 1.28 (1.02–1.77, n = 2284) so there was good fit between the energies detected and the user-defined elements (expected curve). The 55–60 elements that were detected in the scans were reduced to 16 elements that are common to palaeoenvironmental research (e.g., Croudace et al., 2006; Thomson et al., 2006; Gregory et al., 2019) and had sufficiently high intensities (~ $10^2 - 10^5$ cts): Al, Si, S, K, Ca, Ti, V, Cr, Mn, Fe, Cu, Ni, Rb, Sr, Zr, and Ba. Boxplots, which are effective at showing the spread and summary statistics of a dataset, were used to compare the data between each run (n = 4; Fig. 4). The box

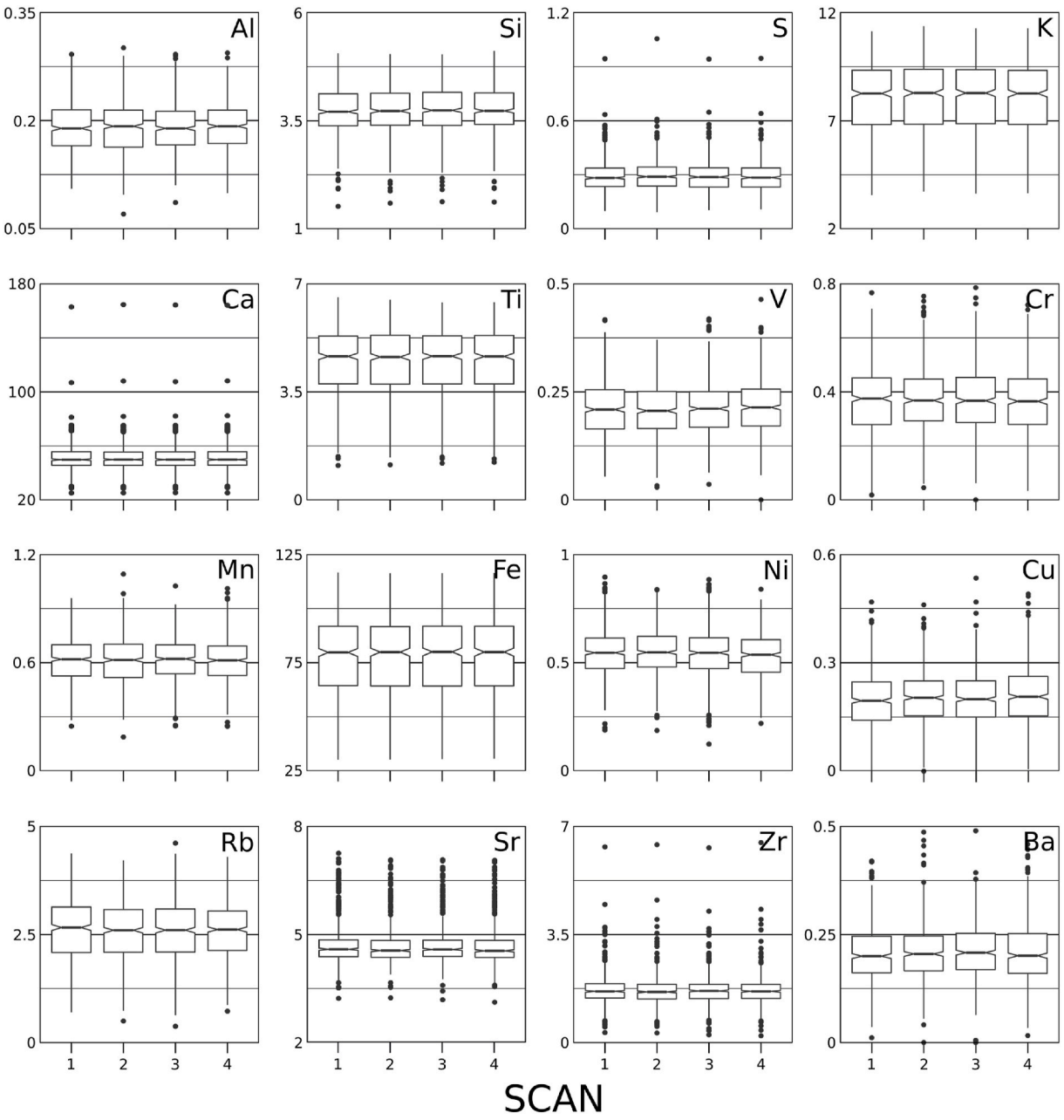

Fig. 4. Boxplots of the elemental data, in kilo-counts (kcts), from scans 1–4 (n = 571 observations per scan). The notch represents the median value and the circles represent outliers. Note that even in elements with greater numbers of outliers (e.g. Ca, Zr, Sr), their values are similar between runs.

(interquartile range; 3Q-1Q) contains 50% of the data, with the median value represented by the notch and any outliers indicated by circles beyond the 'whiskers'. Major elements (K, Ti, Ca, Si, Fe, Sr) all showed less than 1% variation in the median value while Al, Zr, Rb, Cr, Mn, Ni, and S had < 3% variation. The elements V, Cu, and Ba showed the most variation between the median values, although it was still < 5%. Even the elements that showed more outliers, such as Ca, Sr, Zr, and Si, had similar outlier values across all four scans. The near-overlapping median and box range values across the four scans indicates that the true median values are similar (95% confidence interval). Scatterplot comparisons between two scans, using the Spearman-Rho correlation coefficient showed strong to very strong average Spearman correlation ($R^2 > 0.7$) for Sr, S, and Zr, with Fe, Ca, Ti, K, and Si having correlation values greater than 0.96. The remaining elements all showed weak correlations ($R^2 < 0.4$) with increased scatter about the $y = x$ regression line, likely due to the overall lower concentration of these elements (see subsection 3.2).

3.2. ICP-OES/MS elemental concentrations

Lithogeochemistry derived from ICP analysis showed 10 oxides and 45 individual elements. Two of the oxides (MgO and Na_2O) were of elements that are too light for μXRF detection and one (P_2O_5) was not detected so they were excluded from further analysis; combined, these three oxides comprised < 4% of the sample by weight. The remaining oxides (SiO_2, Al_2O_3, TiO_2, Fe_2O_3, K_2O, CaO, and MnO) comprised between 82.6 and 91.77 (median = 87.35) weight percent of the sample, with SiO_2 being the most prevalent (median = 67.47%; 59.32–74.03), followed by Al_2O_3 and CaO, Fe_2O_3 and K_2O, and trace amounts of TiO_2 and MnO. For the remaining elements of interest, Ba had the highest concentration (median = 309 ppm; 269–331), followed closely by Zr (median = 162 ppm; 143–205), Sr (median = 152 ppm; 137–238), and

Rb (median = 87 ppm; 33–109); Cr, V, Ni, and Cu (in order of decreasing concentration) all had median values below 100 ppm.

The ICP data were quite distinct in the two different lithologies. The mudstone intervals had higher concentrations of Al_2O_3 and K_2O, likely incorporated into illite and kaolinite, as well as higher concentrations of TiO_2 and Fe_2O_3, while the sandstone intervals were typically higher in SiO_2 (quartz), CaO, and Zr/Rb. The Zr values on their own did not show a clear correlation to lithology so the Zr/Rb ratio is mainly driven by the

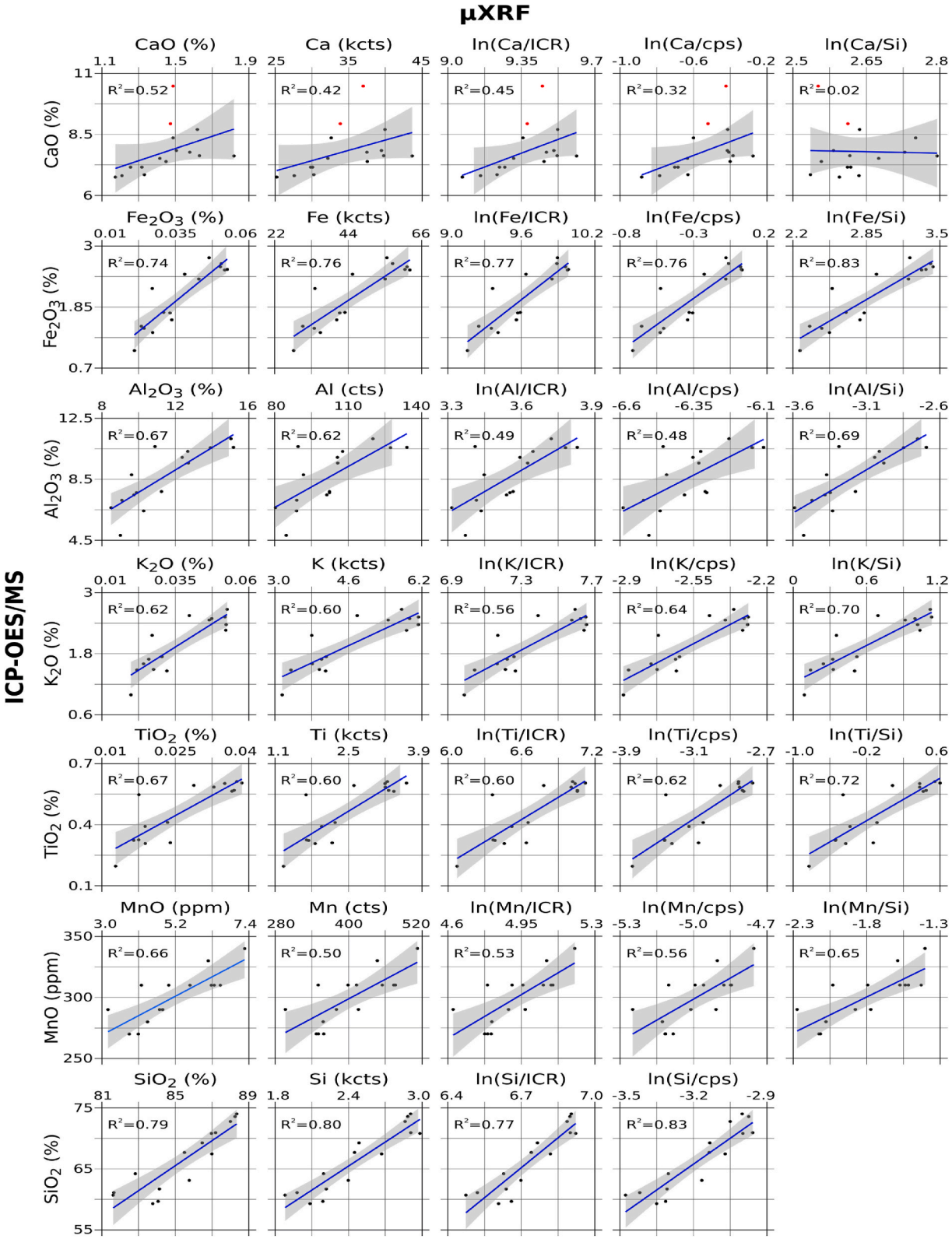

Fig. 5. Bivariate plots of ICP-OES oxide concentrations (y-axes) compared to various calibrations of μXRF data: Cody-shale calibrated (%), QSpec-batched (counts), and log-normalised. Red points in CaO graphs represent the outliers that result in weaker correlations. (For interpretation of the references to colour in this figure legend, the reader is referred to the Web version of this article.)

Rb content, which is consistently at least 50% higher in the mudstone laminae. The mudstone intervals were also less oxygenated overall than the sandstone, as seen in the redox-related proxies MnO/TiO_2, which decreases with lower oxygen conditions in the sediment (Croudace et al., 2006; Thomson et al., 2006), and Redox (sum of V, Cr, and U), which increases with decreasing oxygen in sediments (Dypvik and Harris, 2001; Tribovillard et al., 2006; Ben-Awuah et al., 2017).

3.3. Comparison of ICP-OES/MS to μXRF

Absolute elemental concentrations from ICP analysis were compared to the batched Itrax data, the Cody Shale calibrated data, and log-ratioed (ULC) data to assess the fit between the μXRF elemental intensities and the absolute concentrations obtained through ICP analysis. At each ICP sample depth, the μXRF data were averaged over an 11-point window, centred on the depth (e.g., 8.6 mm, 19.6 mm, etc.), to provide the same number of total observations ($n = 15$) and to account for the ~2–3 mm span of the ICP samples; an 11-pt window is equivalent to 2 mm. While this provides a good way to compare the two datasets, there will still be some discrepancy due to the micro-scale analytical footprint of an Itrax core scanner (~0.8 mm^3) compared to the total coverage of the sub-samples collected for ICP analysis (40–180 mm^3; see section 2). For example, if the lamina is at an oblique angle to the slab surface, then material from different lithologies can be incorporated into the homogenised ICP subsample, which would not be present in the volume of material analysed by μXRF. Similarly, micro-shells and fragments may be present in the lamina, which would be incorporated into the ICP subsample but may not be abundant enough to pass directly beneath the X-ray detector of the core scanner.

Bivariate plots, comparing the ICP- and μXRF-derived oxide data using a linear smoother ($y \sim x$) and Spearman-Rho correlation coefficient, were produced to show the correlation between the two analytical methods (Fig. 5). Most of the oxides (SiO_2, Al_2O_3, TiO_2, Fe_2O_3, and K_2O) showed moderate to strong Spearman-Rho correlation coefficients of $R^2 > 0.6$ between the ICP and μXRF data, whether the μXRF data were calibrated to Cody Shale (wt.% and ppm) or left uncalibrated (counts). The ICP-derived MnO showed a weaker correlation when compared to the uncalibrated data ($R^2 = 0.50$) than when compared to the calibrated data ($R^2 = 0.66$) due to increased scatter about the $y = x$ regression line although a clear linear trend is still apparent in the scatterplots. The CaO concentration showed only moderate correlation for both calibrated and uncalibrated μXRF data ($R^2 = 0.52$ and 0.42, respectively) and had a higher level of scatter about the regression line however, the correlation would be stronger without a few outliers. The removal of the two highest outliers (red points, Fig. 5), corresponding to depths of 60.6 mm and 137.6 mm, yielded R^2 values of 0.67 and 0.62 for calibrated and raw μXRF data, respectively. The Si-log-normalised data showed stronger correlations to the ICP concentrations compared to the uncalibrated and calibrated data for Fe ($R^2 = 0.83$), K ($R^2 = 0.70$), and Ti ($R^2 = 0.72$) but similar values for Al ($R^2 = 0.69$ compared to 0.67) and Mn ($R^2 = 0.65$ compared to 0.66). The relationship between CaO from ICP and Si-log-normalised Ca from μXRF had a near zero correlation ($R^2 = 0.02$), possibly due to the moderate positive correlation ($R = 0.57$) between Ca and Si, compared to the strongly negative ($R = -0.89$ to -0.95) relationship between SiO_2 and the other oxides. Overall, these correlations are similar to those found by Gregory et al. (2019) when analysing modern lake sediments and in some cases better, though direct comparison is not possible as they used Kendall's tau correlations. Since

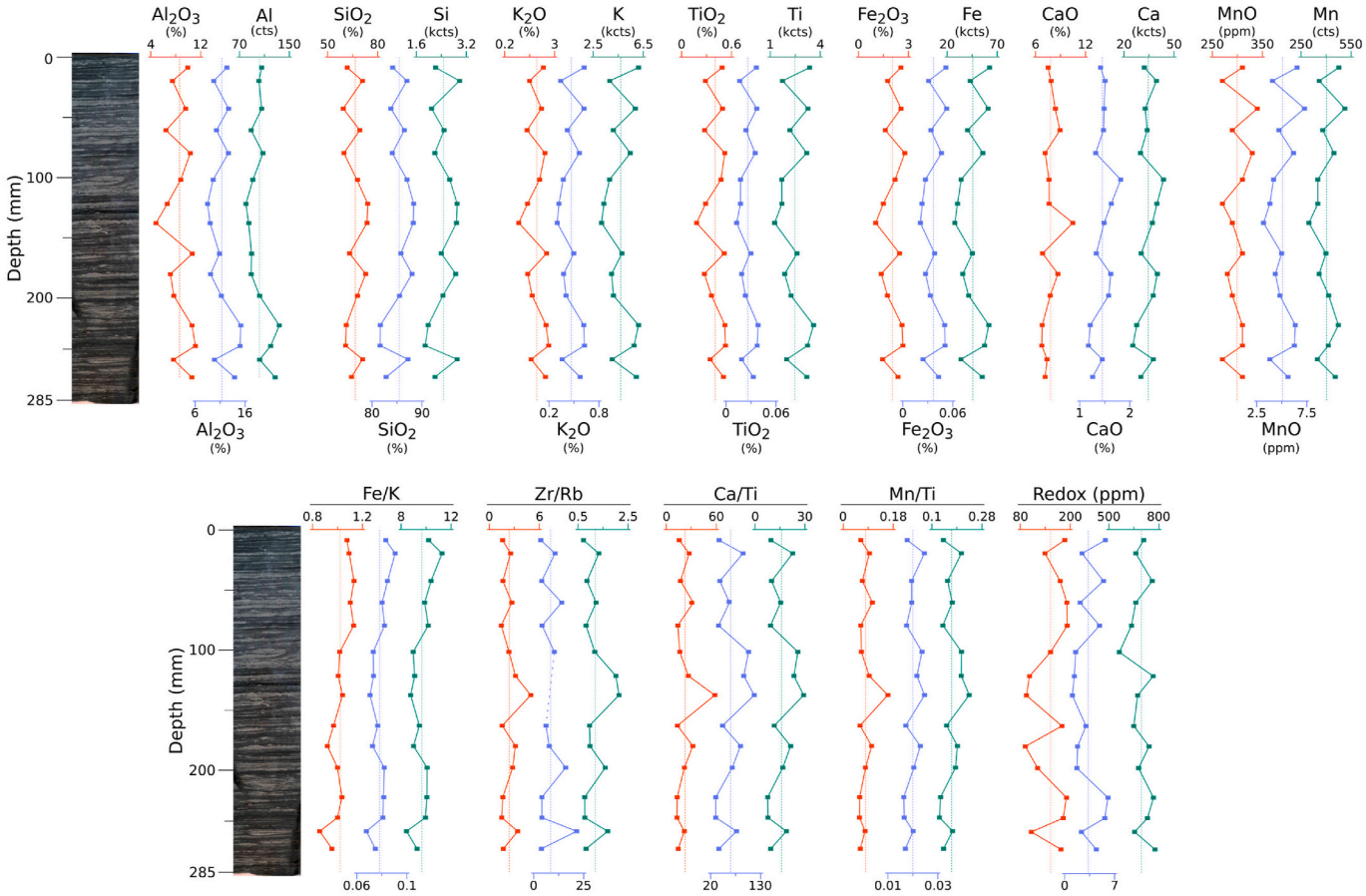

Fig. 6. Oxide and elemental trends for ICP-OES (red), Cody-calibrated μXRF (blue), and batched μXRF (green) data. The Cody-calibrated Zr/Rb had two infinite intervals (121.6 and 137.6 mm) due to zeros in the Rb data so there is a break in the trend. The fine dashed line on each graph represents the mean. (For interpretation of the references to colour in this figure legend, the reader is referred to the Web version of this article.)

none of the calibrations resulted in significantly better correlations for all elements, the uncalibrated μXRF data will be presented for the remainder of the paper. The elemental variation as a function of depth shows that the aliased μXRF data are very similar to the ICP concentrations (relative pattern of variation; Fig. 6). When comparing the Al values, the μXRF data showed an overall smoother curve (less variation) than the ICP data, particularly in the middle six intervals from 100 to 200 mm, and the Cody-calibrated values (Al_2O_3) showed a more distinct trend than the uncalibrated Al. An opposite pattern can be seen in the Ca trends, where the μXRF data display a more prominent trend throughout, although neither Itrax trend produced the same peak at 137.6 mm as the ICP-OES data. To provide a semi-quantitative comparison of the trends, simple confusion matrices were generated to examine how data points shifted relative to their respective means,

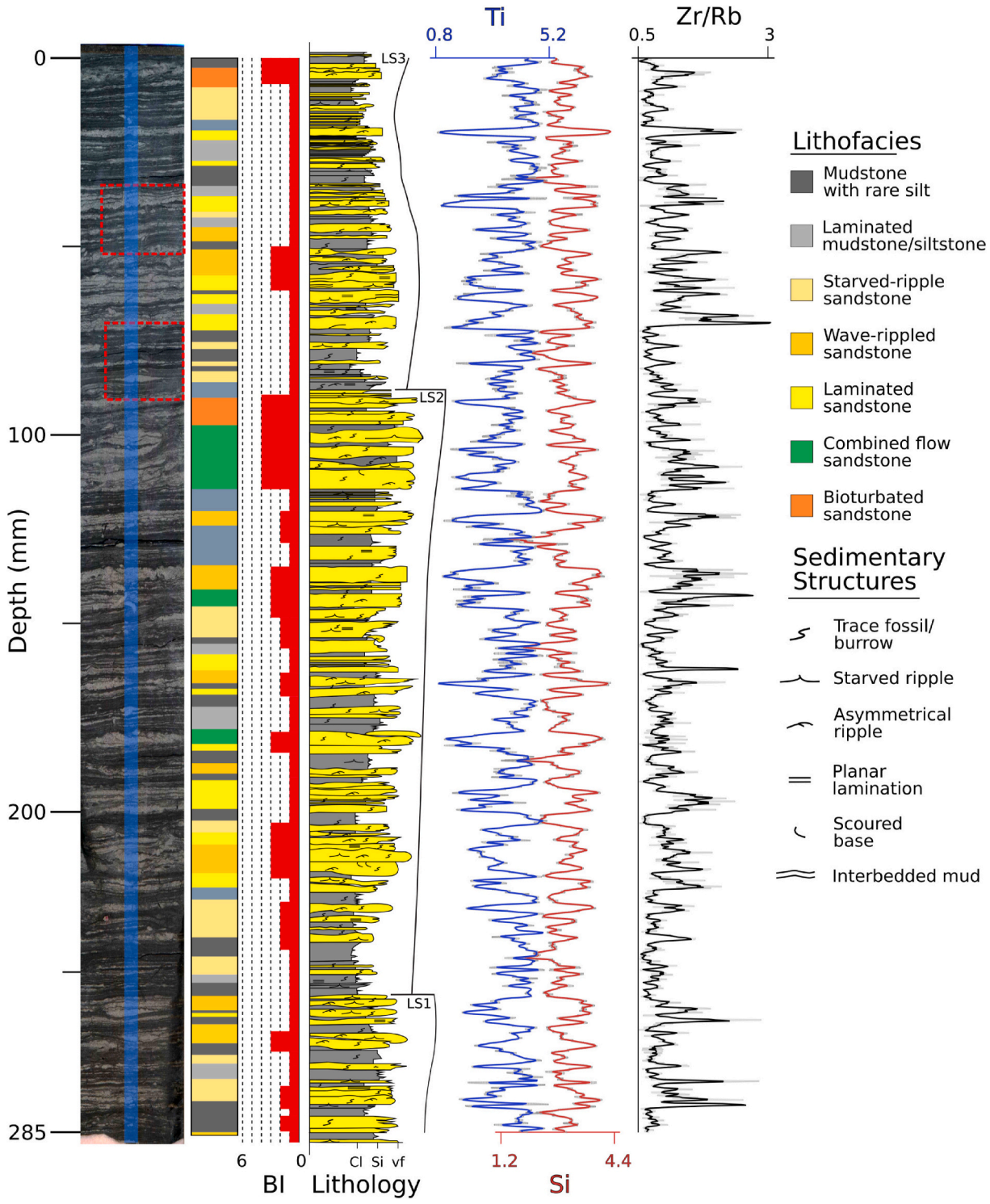

Fig. 7. Core photo, lithofacies, BI, measured section, and μXRF-derived elements and ratios. The negatively-correlated Ti and Si trends closely follow changes in the lithology, with diverging trends associated with coarser-grained laminae. The dashed red boxes correspond to Fig. 8 and the blue band represents the track of the 8 mm wide scanning beam. For the measured section, Cl = clay, Si = silt, and vf = very fine sand. The laminasets (LS1-3) are identified next to the lithology. Values for Ti and Si are in kilo-counts. (For interpretation of the references to colour in this figure legend, the reader is referred to the Web version of this article.)

regardless of the magnitude of that shift. If both datasets moved in the same direction (i.e., increased/decreased) relative to their respective mean then a 1 was assigned, otherwise a zero was assigned; the total 1s and 0s are presented in Table 2. Nearly all of the elements show simultaneous movements in both datasets, with the raw Ca trend showing the least similarity (60%) to the calcium oxide ($CaO_{ICP\text{-}OES}$) trend; however, when the oxide and raw Ca and Ti values are ratioed the trends become more similar (73%). The data sets moving opposite to each other could be the result of sampling errors while preparing material for ICP-OES analysis, which requires a larger sample size, so subtle offsets within the lithology could create discrepancies in the data. However, in the case of 'Redox' (V + Cr + U) the lower correlation is likely a result of the lower overall concentration of these elements (< 100 ppm; see subsection 3.2); a longer exposure time (e.g., 30 s) may increase the correlation of these proxies.

3.4. Lithofacies

Lithologic analysis of the Cheese Slab showed mostly continuous laminae, with a low-angle inclination and preserved sedimentary structures (e.g. ripples, grading, cross-laminations; Fig. 7). Petrographic analysis of thin sections showed that the sandstone laminae were mostly well-sorted and dominated by subangular, very fine sand-to coarse silt-sized quartz grains, with varying amounts of carbonate minerals, including subhedral grains and interstitial cement (Fig. 8). Using X-ray diffraction (XRD) on a different section of the same core block, Yoon et al. (2019) determined that feldspars were also a minor component of the sandstone but they were coated with calcite cement; therefore some of our carbonate grains may in fact be feldspars (see Fig. 8A). Mineral grains in the mudstone were too small for visual identification but XRD analysis (Yoon et al., 2019) indicated these laminae to be dominated by illite and kaolinite, with higher concentrations of organic carbon relative to the quartz-rich sand laminae; Birgenheier et al. (2017) found similar results in their analysis of Blue Gate shale. Organic macerals up to very fine sand size can be observed in most laminae but in the mudstone intervals they also appear as distinct, though discontinuous, sub-millimetre thin beds, possibly settling out of a storm-enhanced fluid mud by flocculation (e.g., Plint, 2014).

Table 2
Confusion matrix results of single and ratioed elements; Redox = V + Cr + U. In the Cody-calibrated μXRF dataset, all but three Rb values were either 1 or 0 so the Zr/Rb trend could not be compared to the ICP trend accurately. Same (1): values (ICP and μXRF) responded the same relative to their respective means; Diverge (0): values responded in opposite directions relative to their respective means.

Single Elements							
Oxides							
	Al_2O_3	SiO_2	K_2O	TiO_2	Fe_2O_3	CaO	MnO
Same	13	14	14	14	14	12	13
Diverge	2	1	1	1	1	3	2
Raw Elements							
	Al	*Si*	*K*	*Ti*	*Fe*	*Ca*	*Mn*
Same	11	14	14	14	13	9	12
Diverge	4	1	1	1	2	6	3
Element Ratios							
Oxides							
	Zr/Rb	*Redox*	CaO/TiO_2	MnO/TiO_2	Fe_2O_3/K_2O		
Same	–	12	11	11	12		
Diverge	–	3	4	4	3		
Raw Elements							
	Zr/Rb	*Redox*	*Ca/Ti*	*Mn/Ti*	*Fe/K*		
Same	14	9	11	12	12		
Diverge	1	6	4	3	3		

Bioturbation throughout the section was low to moderate, with a Bioturbation Index (BI) of 1–4 (mean 2), which is a semi-quantitative measure indicating the ratio between preserved and disturbed sedimentary structures as a result of burrowing infauna. A BI of 0 indicates few or no burrows or trace fossils, BI of 3 indicates roughly 50% of the sedimentary structures (laminae) remain, and a BI of 6 is completely burrowed with no laminae preserved. Trace fossils of *Palaeophycus*, *Teichichnus*, *Planolites*, *Chondrites*, *Helminthopsis*, and *Zoophycos* were identified, which form the *Cruziana* ichnofacies (MacEachern et al., 2010) or the more proximal *Phycosiphon* ichnofacies recently described by MacEachern and Bann (2020), indicative of deposition in the sublittoral zone on a moderate-to low-energy medial shelf. Very rare (~10 total) 'rotalid' and 'bolivinid' type calcareous foraminifera were observed in thin section with good preservation indicating that they were likely part of the living benthos at the time of deposition. The chambers were filled with carbonate cement (Fig. 8C and D) and would produce anomalously high Ca values if the μXRF analysis passed over one directly, which could explain the lesser degree of correlation between the Itrax- and ICP-derived Ca concentrations.

Laminae were characterised and grouped according to their grain size, sedimentary structures, and degree of bioturbation into 7 different microfacies: 1) mudstone with rare silt (29% of the section); 2) mudstone with laminated silt (12%); 3) starved-ripple sandstone (10%); 4) wave-rippled sandstone (17%); 5) combined-flow-rippled sandstone (12%); 6) laminated sandstone (14%); and 7) bioturbated sandstone (6%). Wave ripples were distinguished based on their symmetrical profile and the presence of convex-up cross-laminations, while combined-flow ripples have a slightly asymmetric profile and concave up cross-laminations (Fig. 9); no ripples were observed that showed a highly asymmetric cross-section (i.e., unidirectional current ripple). The presence of cross-laminations and symmetrical and asymmetrical ripples suggests that the sediments were dominated by combined flows. In thin section, the laminae show both normal grading, often with sharp and scoured basal contacts, and inverse grading, with evidence of bioturbation at the upper contact. Some intervals also display inverse-to normal-grading successions that are typical of river-fed hyperpycnal flows, however, the interpreted depth and distance from the shoreline based on the other proxies suggests that these intervals are either very distal expressions of river-fed hyperpycnal flows or they are wave- and current-generated hyperpycnal flows (Bhattacharya and MacEachern, 2009).

Increasing thickness and frequency of sandstone laminae was used to identify laminasets, which have sharp, upper contacts and an increase in wave and combined-flow reworking of the laminae approaching the top of a laminaset. Three laminasets (LS1-3) were identified in the Cheese Slab, though only LS2 is complete. The basal contact of the first laminaset, LS1, is not present but the top contact is visible at ~255 mm, where wave-modified sandstone laminae (Microfacies 4) transition to a mudstone-dominant unit with sparse silt (Microfacies 1). Moving upcore, LS2 shows a complete succession of mudstone with rare silt (Microfacies 1) at the base followed by an overall increase in sandstone laminae and evidence of wave and combined-flow reworking (Microfacies 5) up to 80 mm. Bioturbation, which has been used as a proxy for sedimentation rate (e.g., Bhattacharya et al., 2019, 2020), is higher at the top of LS2 than LS1, including a large *Zoophycos* burrow at 100 mm, indicating a significant decrease in the sedimentation rate, or a possible depositional hiatus, between LS2 and LS3. Laminaset 3, which is also incomplete, shows a more rapid transition from laminated siltstone-mudstone to combined-flow sandstone, with several millimetres at the base of LS3 compared to 30–40 mm at the base of LS2.

Generally, the grading patterns in the lower half of the core are more gradual and complete, with few sharp contacts until the upper few centimetres of LS2. Above 100 mm, the laminae show more fining upward successions with abrupt basal contacts and evidence of scour indicating more frequent, higher energy events. This pattern of fining

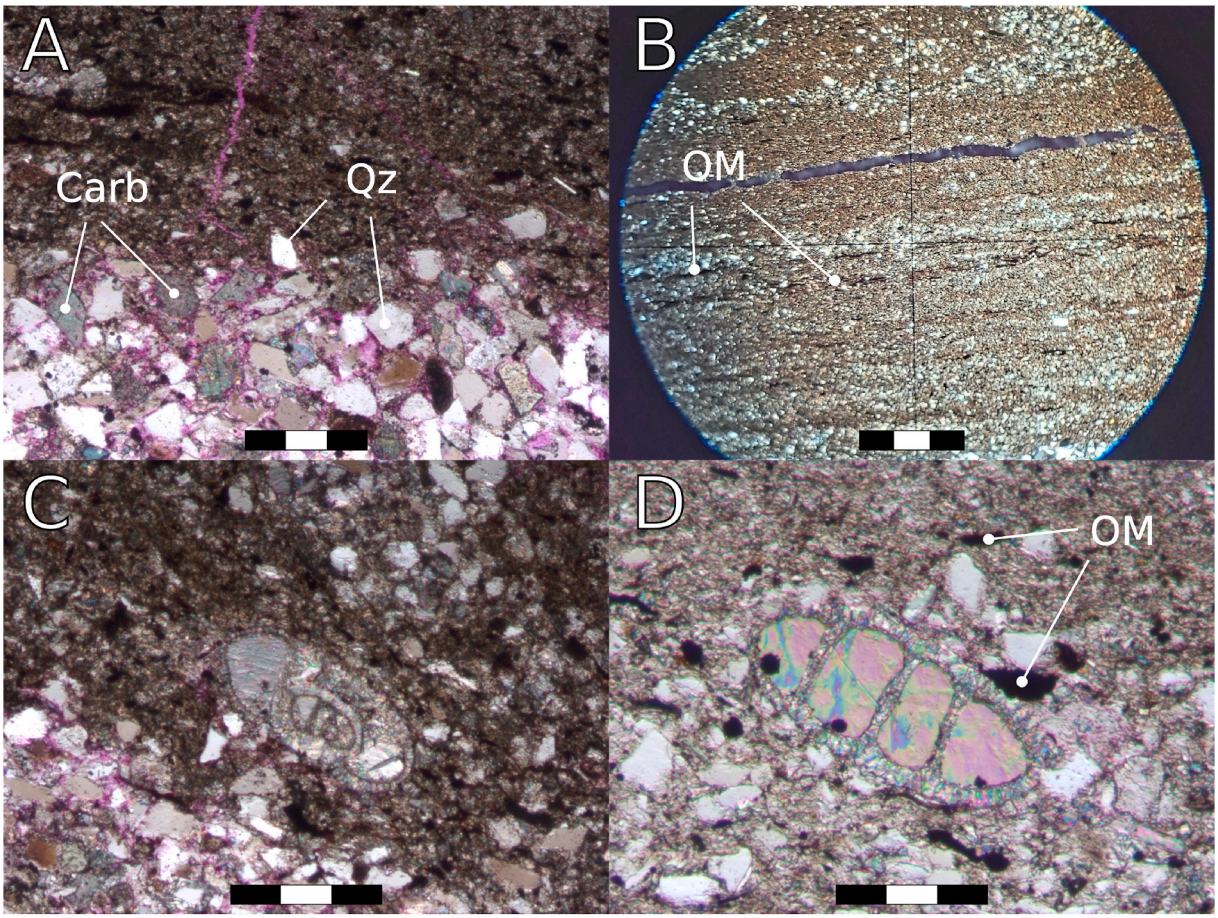

Fig. 8. Thin Section photomicrographs in XPL: A) Grain size and mineral content comparison between the sandstone and mudstone intervals (Carb = Carbonate, Qz = Quartz, scale bar = 0.25 mm). As noted in the text, the carbonate grains may actually be feldspar coated in calcite as seen by Yoon et al. (2019); B) Fine-grained laminations in a siltstone-dominant heterolith (Microfacies 2). The mostly continuous laminations are indicative of the intermediate mudbelt; note the fine organic matter (OM) condensed horizons (scale bar = 1 mm); C-D) Benthic, rotalid calcareous foraminifera with infilled chambers of carbonate cement (scale bars = 0.25 mm).

upward with a sharp basal contact is indicative of an ignitive surge (Mulder et al., 2003), such as a wave-enhanced sediment gravity flow (WESGF; Macquaker et al., 2010), so this could represent a transition to more frequent storms in LS3. However, there is also a decrease in evidence of wave reworking (i.e. more parallel laminations) so the area of deposition may have shifted slightly below storm-wave base. Alternatively, the climatic conditions that existed during the deposition of LS2 may represent a period of above-average storm intensity, thus increasing the depth of storm-wave influence. Since the exact location of the core is unknown we are unable to provide an age but if we assume sedimentation rates of several tenths of a millimetre per year then the core represents roughly 200–300 years, so the climatic conditions of LS2 could be operating on a centennial-scale cycle; this would need to be investigated over a longer section (i.e., a few tens of metres).

4. Discussion

4.1. μXRF and lithology

The μXRF-derived Ti, Si and Zr/Rb curves showed good correlation to the lithology and provided for added interpretation of coarsening- and fining-upward successions (see Fig. 7). In this section, the sandstone intervals had higher Zr/Rb, Si, and Ca values, while mudstone intervals were associated with Fe, Ti, K, and Al. The Zr/Rb ratio is a common grain-size indicator, with increasing values corresponding to coarser-grained sediments due to zirconium being contained in the heavy fraction, predominantly as zircons, while rubidium resides in the clay fraction from weathered aluminosilicates (Wang et al., 2011; Beil et al., 2018). The positive correlation between Si and Ca that we identified was also noticed to occur periodically in a 325 m long continuous succession from the Cretaceous Tarfaya Basin of southern Morocco (Beil et al., 2018). They interpreted these intervals as representing sediment winnowing and subsequent carbonate cementation at the trangressive surface, based on correlation to lithology, stable isotopes, and foraminifera. It is unlikely that the short length of the Cheese Slab is recording that large-scale of an event so the winnowing in our section is likely the result of increased turbulence at the seabed. In addition to identifying the coarsening- and fining-upward successions, the Ti, Si, and Zr/Rb curves provide information regarding the relative grain size changes through the section. The bottom half of the core shows more gradual changes as well as lower overall peaks, especially in the Zr/Rb values, while the upper 75 mm show the sharp basal contacts that are also identified in the lithology. The correlation can also be seen at the microscopic scale where the Ti, Si, and Zr/Rb follow the normal and inverse grading trends and can be used to identify sharp or gradual contacts. Even in cases of increased bioturbation, the underlying gradational trend is visible (see Fig. 9).

Comparing the elemental intensity trends from the μXRF data to thin sections also allowed for a better understanding of the mineralogy (Fig. 10). Since μXRF core scanners are not able to determine the oxidation state of the elements, it is not possible to know the mineral phase they are contained in. For example, Fe can be found as an oxide

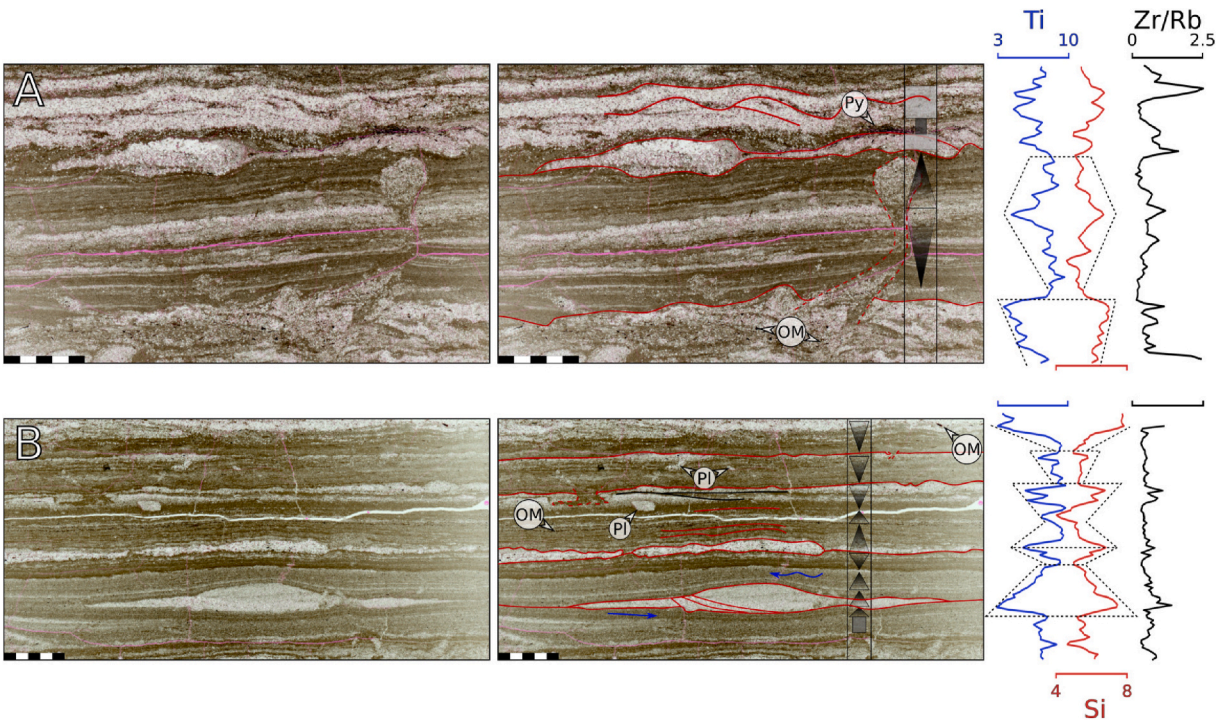

Fig. 9. Sedimentary structures as seen in thin section (plane-polarized light). Dashed red lines indicate burrows and black box indicates location of scan. Notice the presence of combined flow in the starved ripple in B, as indicated by the blue arrows, compared to the undulating tops of wave-modified sediments at the top of A. Pl = *Planolites*, OM = organic matter, Py = Pyrite (see Fig. 10). Ti and Si values are in kilo-counts (kcts). (For interpretation of the references to colour in this figure legend, the reader is referred to the Web version of this article.)

(Fe_2O_3), associated with carbonate as siderite ($FeCO_3$), or associated with sulphur as pyrite (FeS_2) depending on whether it's Fe^{2+} or Fe^{3+} as a result of the redox state in the sediments (Tribovillard et al., 2006; Little et al., 2015). However, comparing multiple elements and ratios allows for an accurate mineralogic composition to be obtained. The peaks in Si/Ti, Ca/Ti, and Mn/Ti ratios match the coarse-grained laminae and indicate an abundance of quartz and carbonate. The mudstone laminae were enriched in Fe, Ti, K, and Al indicating that these elements are being deposited in the clay fraction, mainly as illite and kaolinite, though visual identification of mineral grains in these layers was not possible. There are many thin, opaque laminae composed of organic matter present throughout these layers but in a single location at ~60 mm there is a peak in both the Fe and S/Fe curves indicating the presence of pyrite (i.e., sulfate-reducing conditions). This is a very localised phenomenon so this just indicates that while the benthos was mostly oxic to dysoxic, some areas may have been anoxic to euxinic (see Fig. 9A); this relationship could prove effective at identifying anoxic intervals in longer cores.

4.2. Depositional environment

Both the lithofacies and ichnofacies indicate the depositional environment to be close to, or just below, storm-wave base and influenced by offshore bottom currents. The WIS is thought to be storm dominated, although in any given location we can not be certain how frequently the sea floor was influenced by large storms. Studies of linked river systems by Lin et al. (2019) and Sharma et al. (2017) suggest annual river flood occurences that may have been storm-driven so it is likely that the sea floor was influenced by storm activity on a decadal scale, possibly every few years. Given the ubiquity of burrowing, the presence of benthic foraminifera, and lack of anoxic chemofacies the sediment water interface was oxic, with very localised zones of dysoxic to anoxic conditions, as indicated by the rare presence of pyrite. These localised low oxygen conditions help to explain the low diversity of burrows as well as the preservation of organic matter, as seen in thin section. Depositional mechanisms of sediments are typically interpreted based on the grain size and structures in the laminasets. A complete river-fed hyperpycnite has inverse to normal grading patterns, as flow energy waxes and wanes, and may also show asymmetric ripples. However, differences in flood magnitude, duration, and the distance from shoreline can result in base-truncated (e.g., no inverse grading) sequences, which can then be difficult to distinguish from other event beds (e.g., WESGF, tempestite, turbidite; Mulder et al., 2003; Macquaker et al., 2010; Schieber, 2016)). Our results show that adding chemofacies analysis using μXRF data may help to distinguish between river-fed and remobilised marine sediments due to the high volume of data.

Previous research (e.g., Baumgardner and Rowe, 2017) has applied hierarchical cluster analysis (HCA) to group the elements and provide a rapid and quantitative method to establish chemofacies. For our data, we applied an unsupervised clustering algorithm (self-organising map; SOM) to better understand the principle elemental controls. In a SOM, observations in multi-dimensional space compete for nodes in a grid (tesselation) based on a discriminant function (e.g. Euclidean distance between the node parameters and the observation). The SOM algorithm is iterative so the parameters of each node are continuously re-evaluated as new intervals are assigned. Since the clustering results from the SOM are topologically invariant, it is possible to create hierarchical groupings of nodes based on their topological relationships. In this way, nodes can subsequently be grouped into higher order 'superclusters' and 'ultra--clusters', if desired. We further grouped our observation clusters (n = 169) into k = 5 'superclusters' (Fig. 11). The two main elemental controls on the superclusters were Sr, which was highest in supercluster 1 and correlated with the sandstone laminae, and Fe, which was highest in supercluster 5 and correlated with the mudstone layers. The higher levels of Sr, indicating the presence of aragonite, in the sandy layers shows that these sediments originated from a shallow marine source, rather than directly from a fluvial source, and are therefore likely submarine sediment flows aided by turbulent conditions at the seabed from

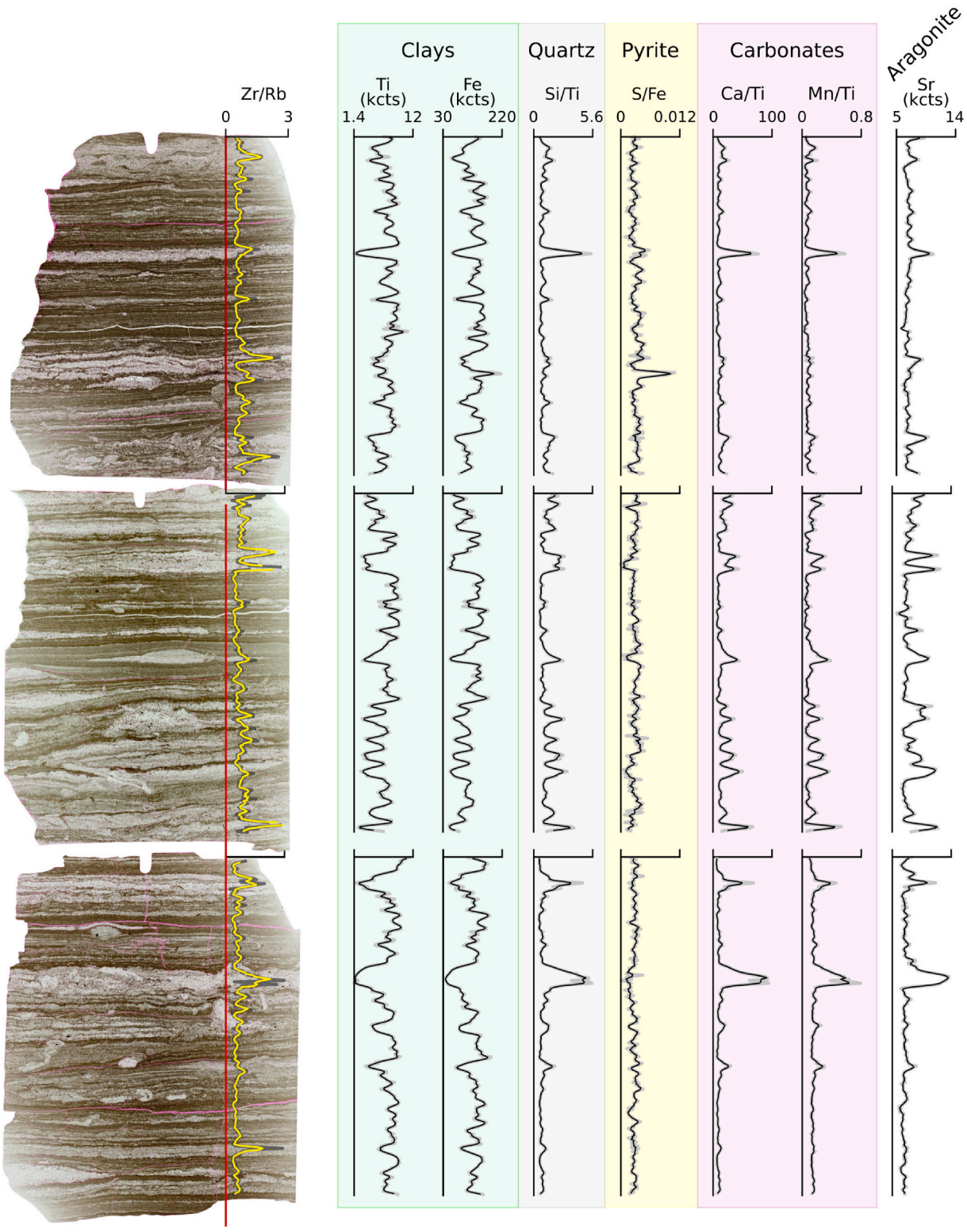

Fig. 10. Comparing the μXRF signature to mineralogy. Scanned thin section images are in plane-polarized light. The peak in S/Fe in the top thin corresponds to the pyrite seen in Fig. 9A.

wave action. Based on the combined characteristics, these sediments were likely deposited in the intermediate mudbelt, at or just below storm wave base (see Fig. 2; cf. Facies 2.4 of Birgenheier et al., 2017 and Microfacies 1 of Plint, 2014). The increase in sharp-based, fining upward successions above 100 mm may indicate a shift to more frequent events and this is supported further by an increase in the Fe/K ratio (see Fig. 6), which would indicate more intense weathering of terrestrial rocks (Zarriess and Mackensen, 2010; Zarriess et al., 2011).

4.3. Implications for petroleum geology

The chemofacies analysis of elemental trends and clusters

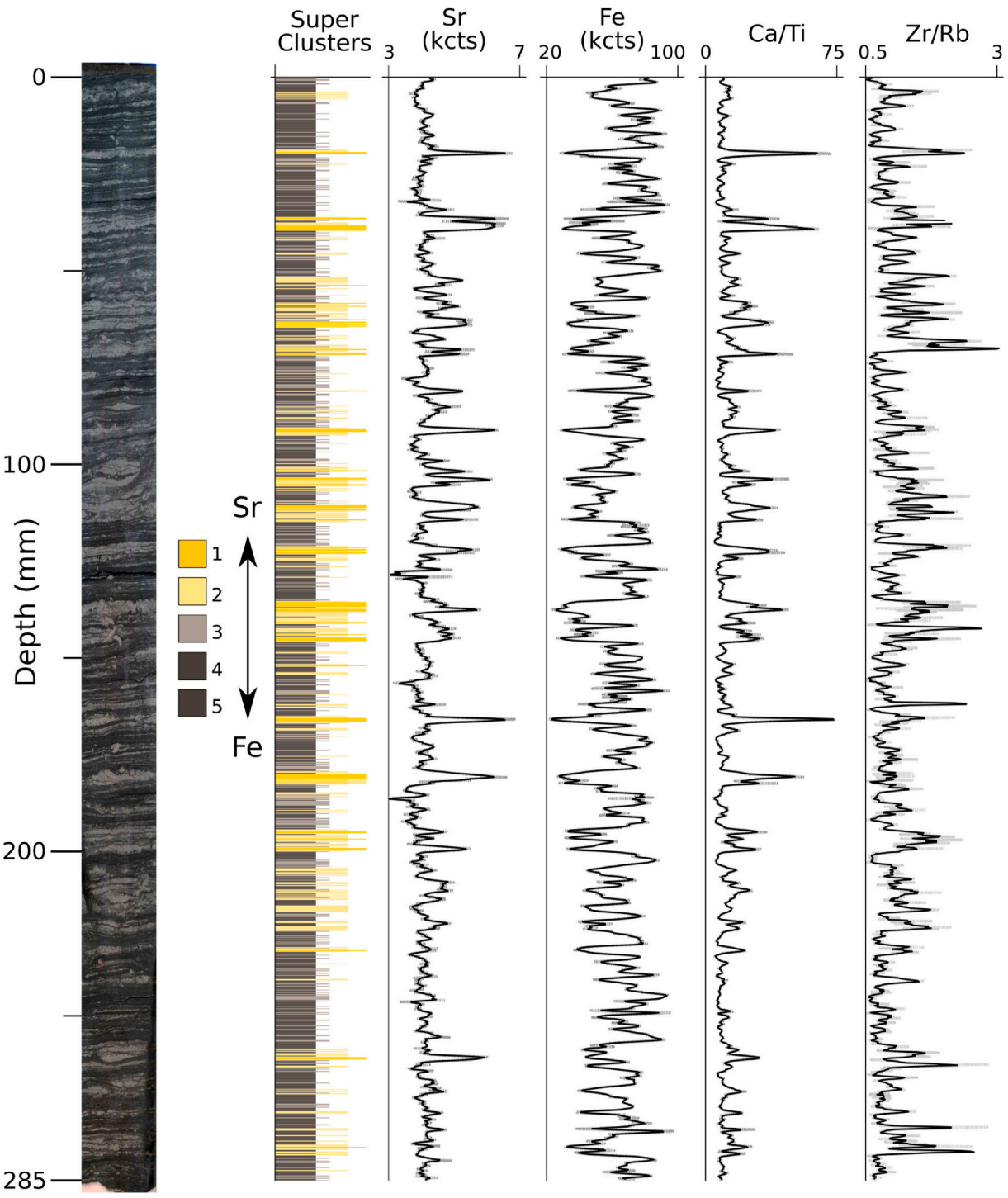

Fig. 11. The supercluster results from the Self-Organising Map. Each interval was assigned to one of 5 superclusters, primarily controlled by Sr and Fe content, but K, Si, and Mn are also included in the decision tree. The superclusters were resized horizontally to indicate relative grain size and coloured to correspond to lithology.

demonstrated promising results for application to hydrocarbon exploration and production. When plotted next to each other, the Ti and Si curves were well correlated with the lithology and mimicked the appearance of wireline logs (gamma and resistivity), which are the foundation of correlating surfaces across a basin. However, the number of elemental proxies, including ratios, and high-resolution vertical sampling obtained from μXRF core scanning allow for a more comprehensive investigation of the facies and have the potential to allow for more precise mapping (see Turner et al., 2016). For example, the presence of increased Sr in the sandstone layers indicates that these sediments were remobilised by wave action from a shallow marine environment as opposed to being directly river-fed, which provides information on the water depth and distance from shoreline. This information can be useful when correlating across multiple cores so as not to correlate a river-fed hyperpycnite with a wave-enhanced sediment gravity flow, which may have a similar lithology in the rock record.

Understanding the mechanical properties of fine-grained rock is an important factor in efficient hydrocarbon extraction as the mechanical strength, which increases with increased carbonate and silica cement, influences the geometry and extent of hydraulically induced fractures.

Weaker, softer mudstones exhibit ductile deformation and may cause induced fractures to close due to rock creep. Yoon et al. (2019) investigated the mechanical properties of the macro- and microfacies and their correlation to grain size and mineralogic composition. They found that XRD analysis, which is industry standard for assessing whether rocks will exhibit brittle or ductile deformation, lacks the resolution to characterise mudstones due to internal heterogeneity of micro-lithofacies. Our results show that μXRF analysis has the resolution needed to rapidly characterise the microfacies of very fine sandstone and mudstone based on relative grain size and composition, which would be beneficial in the planning of hydraulic fracturing activities.

Finally, superclustering with an unsupervised SOM shows promise for identifying significant boundaries, such as flooding surfaces, as well as providing information regarding sediment provenance (terrigenous vs. marine). By applying this method to the entire dataset first and then investigating the 'choices' made by the algorithm using a decision tree, the researcher is given a more complete characterisation of the chemofacies but still has the ability to use previous knowledge to interpret depositional mechanisms and environments. Our superclusters corresponded to visual changes in lithology when plotted by depth and resized and coloured based on comparison to the core. This method will need to be investigated further, first on longer successions and then to other cores laterally, to understand it's potential effectiveness at identifying regional bounding surfaces.

5. Conclusion

The data obtained from fine-grained sedimentary rock using an Itrax μXRF core scanner showed the same high level of reproducibility as previously demonstrated on soft sediment cores, with some major elements even demonstrating direct correlation between separate scans (Ca and Fe; $R^2 = 1$). The common elements Al, Ti, K, Fe, Si, Ca, and Mn showed moderate to strong Spearman correlation coefficients when compared to ICP-OES concentrations and both datasets showed similar down-core trends. The elements Cr, V, Ni, and Cu did not have as strong of a correlation due to their low concentrations (< 100 ppm). Overall, there was no significant impact to the correlation between μXRF elemental intensities and ICP-derived concentrations after calibrating the μXRF data using a variety of techniques. When the data trends (i.e., the positive or negative shift relative to the respective means) were compared using a simple confusion matrix, the correlations were stronger, with most of the elements moving in the same direction in each dataset in more than 80% of the samples.

The elemental signatures obtained from an Itrax μXRF core scanner showed strong correlation to the lithology and mineralogy at both a macroscopic and microscopic scale. The Ti and Si records, which were negatively correlated, effectively tracked lithology changes and could indicate sharp and gradational contacts, particularly when coupled with the Zr/Rb curve. When the data were clustered, a lower frequency signal was also evident indicating that the application of this method to longer successions of Mancos Shale could allow for a more accurate reconstruction of climatic and environmental changes within the Western Interior Seaway through the Upper Cretaceous. The μXRF data also provided added information regarding the mineralogic composition, showing that the sandstone layers had increased levels of Ca and Mn (as carbonates) and Sr (aragonite), indicating they had a shallow marine source. Therefore, it is likely that these laminae are recording submarine flows as a result of wave energy (e.g. WESGFs or tempestites) rather than direct input from river-fed hyperpycnites. In order to resolve these successions even further, palaeocurrent and bathymetric data would be required to determine whether the sediments flowed directly down slope or obliquely.

Our results indicate that fine-grained sedimentary rocks are ideal for palaeoenvironmental reconstructions using μXRF-derived elemental abundances as they minimise the sources of error caused by matrix effects in unconsolidated sediments such as organic matter, pore space, and water content. Additionally, fine-grained sediments from deeper basins typically display a more complete record than proximal, coarser-grained sequences as they do not undergo erosion or depositional hiatuses as frequently. The elemental trends and ratios used in this study were able to provide accurate information about petrography, depositional processes (turbidites, WESGFs), and environmental changes recorded in the mudstone succession at a significantly lower cost and analysis time. A single scan with the Itrax provided $n = 1425$ observations and was completed in less than 6 h for ~$150 USD compared to approximately three weeks and ~$1300 USD required to prepare and analyse $n = 15$ samples with ICP-OES/MS. The high-resolution trends will also allow for more accurate correlation of climatic conditions across other Upper Cretaceous epeiric seas, thus improving our understanding of the climate system in a hothouse world.

Author contributions

JJ Gabriel: Conceptualization, Methodology, Software, Formal Analysis, Investigation, Data Curation, Writing - Original Draft, Visualization. **EG Reinhardt**: Conceptualization, Investigation, Writing - Review/Editing, Supervision. **JP Bhattacharya**: Conceptualization, Investigation, Resources, Writing - Review/Editing, Supervision, Funding acquistion. **X Chang**: Formal Analysis, Investigation.

Funding

Funding for this project was generously supplied by NSERC CRD Grant (CRDPJ-499420-2016) to JP Bhattacharya, jointly sponsored by BP and by the Susan Cunningham Research Chair in Geology at McMaster University, and through an Ontario Graduate Scholarship to JJ Gabriel.

Data availability

Datasets related to this article can be found at https://doi.org/10.17632/9gppkbx58g.1 hosted at Mendeley Data (Gabriel et al., 2022).

Declaration of competing interest

The authors declare that they have no known competing financial interests or personal relationships that could have appeared to influence the work reported in this paper.

Acknowledgements

The authors would like to acknowledge the New Mexico Institute of Mining and Technology and Sandia National Laboratories for providing us with the section of quarried block that we used in this study. Thanks also goes to M. Ouellette at Brock University, Canada, for preparing and cutting the final slab that was used for analysis. Finally, we would like to thank A. Paez at McMaster University, Canada, for valuable assistance with R code and the clustering algorithm.

References

Ahmed, S., Bhattacharya, J.P., Garza, D.E., Li, Y., 2014. Facies Architecture and Stratigraphic Evolution of A River-Dominated Delta Front, Turonian Ferron Sandstone, Utah, U.S.A. J. Sediment. Res. 84, 97–121, 10.2110/jsr.2014.6. http://jsedres.sepmonline.org/cgi/doi/10.2110/jsr.2014.6.

Akyuz, I., Warny, S., Famubode, O., Bhattacharya, J.P., 2016. Palynology of the Upper Cretaceous (Turonian) Ferron Sandstone Member, Utah, USA: Identification of marine flooding surfaces and Milankovitch cycles in subtropical, ever-wet, paralic to non-marine palaeoenvironments. Palynology 40, 122–136. https://doi.org/10.1080/01916122.2015.1014525, 10.1080/01916122.2015.1014525.

Al Maliki, A., Al-lami, A.K., Hussain, H.M., Al-Ansari, N., 2017. Comparison between inductively coupled plasma and X-ray fluorescence performance for Pb analysis in environmental soil samples. Environ. Earth Sci. 76, 1–7. https://doi.org/10.1007/s12665-017-6753-z.

Algeo, T.J., Rowe, H., 2012. Paleoceanographic applications of trace-metal concentration data. Chem. Geol. 324–325, 6–18. https://doi.org/10.1016/j.chemgeo.2011.09.002, 10.1016/j.chemgeo.2011.09.002.

Arenas-Islas, D., Huerta-Diaz, M.A., Norzagaray-López, C.O., Mejia-Piña, K.G., Valdivieso-Ojeda, J.A., Otero, X.L., Arcega-Cabrera, F., 2019. Calibration of portable X-ray fluorescence equipment for the geochemical analysis of carbonate matrices. Sediment. Geol. 391, 105517. https://doi.org/10.1016/j.sedgeo.2019.105517, 10.1016/j.sedgeo.2019.105517.

Armstrong, R.L., 1968. Sevier Orogenic Belt in Nevada and Utah. Geol. Soc. Am. Bull. 79, 429–458.

Baioumy, H., Lehmann, B., 2017. Anomalous enrichment of redox-sensitive trace elements in the marine black shales from the Duwi Formation, Egypt: Evidence for the late Cretaceous Tethys anoxia. J. Afr. Earth Sci. 133, 7–14. https://doi.org/10.1016/j.jafrearsci.2017.05.006, 10.1016/j.jafrearsci.2017.05.006.

Baumgardner, R.W., Rowe, H., 2017. PS Using Hierarchical Cluster Analysis to Improve Facies Definitions in Permian Mudrocks (Wolfcamp and Lower Leonard), Midland Basin, Texas. Geochemistry 23, 2198–2213.

Beil, S., Kuhnt, W., Holbourn, A.E., Aquit, M., Flögel, S., Chellai, E.H., Jabour, H., 2018. New insights into Cenomanian paleoceanography and climate evolution from the Tarfaya Basin, southern Morocco. Cretac. Res. 84, 451–473. https://doi.org/10.1016/j.cretres.2017.11.006.

Ben-Awuah, J., Padmanabhan, E., Sokkalingam, R., 2017. Geochemistry of Miocene sedimentary rocks from offshore West Baram Delta, Sarawak Basin, Malaysia, South China Sea: implications for weathering, provenance, tectonic setting, paleoclimate and paleoenvironment of deposition. Geosci. J. 21, 167–185. https://doi.org/10.1007/s12303-016-0056-3.

Bhattacharya, J., 2010. Deltas. In: James, N., Dalrymple, R. (Eds.), Facies Models 4. Canadian Sedimentology Research Group, St. John's, Newfoundland, pp. 233–264.

Bhattacharya, J.J.P., Miall, A.D., Ferron, C., Gabriel, J., Randazzo, N., Kynaston, D., Jicha, B.B.R., Singer, B.B.S., 2019. Time-stratigraphy in point sourced river deltas: Application to sediment budgets, shelf construction, and paleo-storm records. Earth Sci. Rev. 199, 102985. https://doi.org/10.1016/j.earscirev.2019.102985, 10.1016/j.earscirev.2019.102985.

Bhattacharya, J.P., Howell, C.D., Maceachern, J.A., Walsh, J.P., 2020. Bioturbation , sedimentation rates , and preservation of flood events in deltas. Palaeogeogr. Palaeoclimatol. Palaeoecol. 560. https://doi.org/10.1016/j.palaeo.2020.110049, 10.1016/j.palaeo.2020.110049.

Bhattacharya, J.P., MacEachern, J.A., 2009. Hyperpycnal rivers and prodeltaic shelves in the cretaceous seaway of North America. J. Sediment. Res. 79, 184–209. https://doi.org/10.2110/jsr.2009.026.

Birgenheier, L.P., Horton, B., McCauley, A.D., Johnson, C.L., Kennedy, A., 2017. A depositional model for offshore deposits of the lower Blue Gate Member, Mancos Shale, Uinta Basin, Utah, USA. Sedimentology 64, 1402–1438. https://doi.org/10.1111/sed.12359.

Boggs Jr., S., Boggs, S., 2009. Petrology of Sedimentary Rocks. Cambridge University Press.

Boyle, J.F., Chiverrell, R.C., Schillereff, D., 2015. Approaches to Water Content Correction and Calibration for µXRF Core Scanning: Comparing X-ray Scattering with Simple Regression of Elemental Concentrations. In: Croudace, I.W., Rothwell, R.G. (Eds.), *Micro-XRF Studies of Sediment Cores: Applications of a Non-destructive Tool for the Environmental Sciences* Chapter 14, Developmen ed. Springer Science+Business Media, Dordrecht, pp. 373–390.

Broadhead, R.F., 2015. The Upper Mancos Shale in the San Juan Basin: three plays, conventional and unconventional. AAPG Search Discover. 10791, 39.

Brown, E.T., Johnson, T.C., Scholz, C.A., Cohen, A.S., King, J.W., 2007. Abrupt change in tropical African climate linked to the bipolar seesaw over the past 55,000 years. Geophys. Res. Lett. 34, 1–5. https://doi.org/10.1029/2007GL031240.

Chen, H.F., Yeh, P.Y., Song, S.R., Hsu, S.C., Yang, T.N., Wang, Y., Chi, Z., Lee, T.Q., Chen, M.T., Cheng, C.L., Zou, J., Chang, Y.P., 2013. The Ti/Al molar ratio as a new proxy for tracing sediment transportation processes and its application in aeolian events and sea level change in East Asia. J. Asian Earth Sci. 73, 31–38. https://doi.org/10.1016/j.jseaes.2013.04.017, 10.1016/j.jseaes.2013.04.017.

Craigie, N., 2018. Principles of Elemental Chemostratigraphy: A Practical User Guide. Springer International Publishing AG.

Croudace, I.W., Rindby, A., Rothwell, R.G., 2006. ITRAX: Description and Evaluation of a New Multi-Function X-Ray Core Scanner, vol. 267. Geological Society Special Publication, pp. 51–63. https://doi.org/10.1144/GSL.SP.2006.267.01.04.

Croudace, I.W., Rothwell, R.G. (Eds.), 2015. Micro-XRF Studies of Sediment Cores: Applications of a Non-destructive Tool for the Environmental Sciences. Springer Science+Business Media. http://scholar.google.com/scholar?hl=en&btnG=Search&q=intitle:Developments+in+Paleoenvironmental+Research#8.

Dypvik, H., Harris, N.B., 2001. Geochemical facies analysis of fine-grained siliciclastics using Th/U, Zr/Rb and (Zr + Rb)/Sr ratios. Chem. Geol. 181, 131–146. https://doi.org/10.1016/S0009-2541(01)00278-9.

El-Attar, A., Pranter, M.J., 2016. Regional stratigraphy, elemental chemostratigraphy, and organic richness of the NiobraraMember of the Mancos Shale, Piceance Basin, Colorado. AAPG (Am. Assoc. Pet. Geol.) Bull. 100, 345–377. https://doi.org/10.1306/12071514127.

Eldrett, J.S., Ma, C., Bergman, S.C., Lutz, B., Gregory, F.J., Dodsworth, P., Phipps, M., Hardas, P., Minisini, D., Ozkan, A., Ramezani, J., Bowring, S.A., Kamo, S.L., Ferguson, K., Macaulay, C., Kelly, A.E., 2015. An astronomically calibrated stratigraphy of the Cenomanian, Turonian and earliest Coniacian from the Cretaceous Western Interior Seaway, USA: Implications for global chronostratigraphy. Cretac. Res. 56, 316–344. https://doi.org/10.1016/j.cretres.2015.04.010.

Ernst, T., Berman, T., Buscaglia, J., Eckert-Lumsdon, T., Hanlon, C., Olsson, K., Palenik, C., Ryland, S., Trejos, T., Valadez, M., Almirall, J.R., 2014. Signal-to-noise ratios in forensic glass analysis by micro X-ray fluorescence spectrometry. X Ray Spectrom. 43, 13–21. https://doi.org/10.1002/xrs.2437.

Gabriel, J.J., Reinhardt, E.G., Chang, X., Bhattacharya, J.P., 2022. Application of µXRF analysis on the Upper Cretaceous Mancos Shale: A comparison with ICP-OES/MS: Datasets, 10.17632/9gppkbx58g.1. https://doi.org/10.17632/9gppkbx58g.1.

Gregory, B.R., Patterson, R.T., Reinhardt, E.G., Galloway, J.M., Roe, H.M., 2019. An evaluation of methodologies for calibrating Itrax X-ray fluorescence counts with ICP-MS concentration data for discrete sediment samples. Chem. Geol. 521, 12–27. https://doi.org/10.1016/j.chemgeo.2019.05.008, 10.1016/j.chemgeo.2019.05.008.

Haq, B.U., Huber, B.T., 2017. Anatomy of a eustatic event during the Turonian (Late Cretaceous) hot greenhouse climate. Sci. China Earth Sci. 60, 20–29. https://doi.org/10.1007/s11430-016-0166-y.

Haug, G.H., Günther, D., Peterson, L.C., Sigman, D.M., Hughen, K.A., Aeschlimann, B., 2003. Climate and the Collapse of Maya Civilization. Science 299, 1731–1735. https://doi.org/10.2307/482941.

Hawkins, S.J., Charpentier, R.R., Schenk, C.J., Leathers-Miller, H.M., Klett, T.R., Brownfield, M.E., Finn, T.M., Gaswirth, S.B., Marra, K.R., Le, P.A., Mercier, T.J., Pitman, J.K., Tennyson, M.E., 2016. Assessment of Continuous (Unconventional) Oil and Gas Resources in the Late Cretaceous Mancos Shale of the Piceance Basin, Uinta-Piceance Province, Colorado and Utah. Technical Report June USGS, 2016.

Hubert, J.F., Butera, J.G., Rice, R.F., 1972. Sedimentology of Upper Cretaceous Cody-Parkman Delta, Southwestern Powder River Basin, Wyoming. Geol. Soc. Am. Bull. 83, 1649–1670.

Joo, Y.J., Sageman, B.B., 2014. Cenomanian to campanian carbon isotope chemostratigraphy from the Western Interior Basin, U.S.A. J. Sediment. Res. 84, 529–542. https://doi.org/10.2110/jsr.2014.38.

Kelloway, S.J., Ward, C.R., Marjo, C.E., Wainwright, I.E., Cohen, D.R., 2014. Quantitative chemical profiling of coal using core-scanning X-ray fluorescence techniques. Int. J. Coal Geol. 128–129, 55–67. https://doi.org/10.1016/j.coal.2014.04.006.

Li, Y., Bhattacharya, J.P., 2013. Facies-Architecture Study of A Stepped, Forced Regressvie Compound Incised Valley In the Ferron Notom Delta, Southern Central Utah, U.S.A. J. Sediment. Res. 83, 206–225, 10.2110/jsr.2013.19. http://jsedres.sepmonline.org/cgi/doi/10.2110/jsr.2013.19.

Li, Z., Schieber, J., 2018. Detailed facies analysis of the Upper Cretaceous Tununk Shale Member, Henry Mountains Region, Utah: Implications for mudstone depositional models in epicontinental seas. Sediment. Geol. 364, 141–159. https://doi.org/10.1016/j.sedgeo.2017.12.015, 10.1016/j.sedgeo.2017.12.015.

Lin, W., Bhattacharya, J.P., Stockford, A., 2019. High-resolution Sequence Stratigraphy and Implications For Cretaceous Glacioeustasy of the Late Cretaceous Gallup System, New Mexico, U.S.A. J. Sediment. Res. 89, 552–575. https://doi.org/10.2110/jsr.2019.32.

Little, S.H., Vance, D., Lyons, T.W., McManus, J., 2015. Controls on trace metal authigenic enrichment in reducing sediments: Insights from modern oxygen-deficient settings. Am. J. Sci. 315, 77–119. https://doi.org/10.2475/02.2015.01.

Löwemark, L., Bloemsma, M., Croudace, I., Daly, J.S., Edwards, R.J., Francus, P., Galloway, J.M., Gregory, B.R., Huang, J.-J.S., Jones, A.F., Kylander, M., Luo, Y., Maclachlan, S., Ohlendorf, C., Patterson, R.T., Pearce, C., Profe, J., Reinhardt, E.G., Stranne, C., Tjallingii, R., Turner, J.N., Steven Huang, J.J., Jones, A.F., Kylander, M., Luo, Y., Maclachlan, S., Ohlendorf, C., Patterson, R.T., Pearce, C., Profe, J., Reinhardt, E.G., Stranne, C., Tjallingii, R., Turner, J.N., 2019. Practical guidelines and recent advances in the Itrax XRF core-scanning procedure. Quat. Int. 514, 16–29. https://doi.org/10.1016/j.quaint.2018.10.044, 10.1016/j.quaint.2018.10.044.

Lowery, C.M., Leckie, R.M., Bryant, R., Elderbak, K., Parker, A., Polyak, D.E., Schmidt, M., Snoeyenbos-West, O., Sterzinar, E., 2018. The Late Cretaceous Western Interior Seaway as a model for oxygenation change in epicontinental restricted basins. Earth Sci. Rev. 177, 545–564. https://doi.org/10.1016/j.earscirev.2017.12.001, 10.1016/j.earscirev.2017.12.001.

Ma, C., Meyers, S.R., Sageman, B.B., Singer, B.S., Jicha, B.R., 2014. Testing the astronomical time scale for oceanic anoxic event 2, and its extension into Cenomanian strata of the Western Interior Basin (USA). Bull. Geol. Soc. Am. 126, 974–989. https://doi.org/10.1130/B30922.1.

MacEachern, J.A., Bann, K.L., 2020. The Phycosiphon ichnofacies and the Rosselia ichnofacies: Two new ichnofacies for marine deltaic environments. J. Sediment. Res. 90, 855–886. https://doi.org/10.2110/JSR.2020.41.

MacEachern, J.A., Pemberton, S.G., Gingras, M.K., Bann, K.L., 2010. Ichnology and Facies Models. In: James, N.P., Dalrymple, R.W. (Eds.), *Facies Models 4* Chapter 3. Geological Association of Canada, pp. 19–58.

Macquaker, J.H.S., Bentley, S.J., Bohacs, K.M., 2010. Wave-enhanced sediment-gravity flows and mud dispersal across continental shelves: Reappraising sediment transport processes operating in ancient mudstone successions. Geology 38, 947–950. https://doi.org/10.1130/G31093.1.

McDonough, K.J., Cross, T.A., 1991. Late Cretaceous Sea Level From a Paleoshoreline. J. Geophys. Res. 96, 6591–6607.

Miall, A.D., Catuneanu, O., Vakarelov, B.K., Post, R., 2008. The Western Interior Basin. In: Miall, A.D. (Ed.), *The Sedimentary Basins of the United States and Canada* Chapter Chapter 9. Elsevier, pp. 330–362. https://doi.org/10.1016/S1874-5997(08)00023-3.

Molenaar, C.M., Cobban, W.A., 1991. Middle Cretaceous Stratigraphy on the South and East Sides of the Uinta Basin, Northeastern Utah and Northwestern Colorado. Technical Report U.S. Geological Survey.

Mulder, T., Syvitski, J.P., Migeon, S., Faugères, J.C., Savoye, B., 2003. Marine hyperpycnal flows: Initiation, behaviorand related deposits. A review. Mar. Petrol. Geol. 20, 861–882. https://doi.org/10.1016/j.marpetgeo.2003.01.003.

Peti, L., Augustinus, P.C., Gadd, P.S., Davies, S.J., 2019. Towards characterising rhyolitic tephra layers from New Zealand with rapid, non-destructive μ-XRF core scanning. Quat. Int. 514, 161–172. https://doi.org/10.1016/j.quaint.2018.06.039, 10.1016/j.quaint.2018.06.039.

Plint, A.G., 2014. Mud dispersal across a Cretaceous prodelta: Storm-generated, wave-enhanced sediment gravity flows inferred from mudstone microtexture and microfacies. Sedimentology 61, 609–647. https://doi.org/10.1111/sed.12068.

Plint, A.G., Macquaker, J.H.S., Varban, B.L., 2012. Bedload Transport of Mud Across A Wide, Storm-Influenced Ramp: Cenomanian-Turonian Kaskapau Formation, Western Canada Foreland Basin. J. Sediment. Res. 82, 801–822. https://doi.org/10.2110/jsr.2012.64.

Ridgley, J.L., Condon, S.M., Hatch, J.R., 2013. Geology and Oil and Gas Assessment of the Mancos-Menefee Composite Total Petroleum System, San Juan Basin, New Mexico and Colorado. In: Total Petroleum Systems and Geologic Assessment of Undiscovered Oil and Gas Resources in the San Juan Basin Province, Exclusive of Paleozoic Rocks, p. 97. *New Mexico and Colorado* USGS DDS-69-F (chapter 4).

Rothwell, R.G. (Ed.), 2006. New Techniques in Sediment Core Analysis. Geological Society of London.

Rothwell, R.G., Croudace, I.W., 2015. Micro-XRF Studies of Sediment Cores: A perspective on Capability and Application in the Environmental Sciences. In: Croudace, I.W., Rothwell, R.G. (Eds.), *Micro-XRF Studies of Sediment Cores: Applications of a Non-destructive Tool for the Environmental Sciences* Chapter 1, Developmen ed. Springer Science+Business Media, pp. 1–22.

Rothwell, R.G., Rack, F.R., 2006. New techniques in sediment core analysis: an introduction. In: Rothwell, R. (Ed.), *New Techniques in Sediment Core Analysis* Chapter 1. Geological Society of London volume Special Pu, pp. 1–29. https://doi.org/10.1144/GSL.SP.2006.267.01.01 arXiv:arXiv:1011.1669vol. 3.

Rowe, H., Hughes, N., Robinson, K., 2012. The quantification and application of handheld energy-dispersive x-ray fluorescence (ED-XRF) in mudrock chemostratigraphy and geochemistry. Chem. Geol. 324–325, 122–131. https://doi.org/10.1016/j.chemgeo.2011.12.023.

Schieber, J., 2016. Mud re-distribution in epicontinental basins - Exploring likely processes. Mar. Petrol. Geol. 71, 119–133. https://doi.org/10.1016/j.marpetgeo.2015.12.014, 10.1016/j.marpetgeo.2015.12.014.

Schober, P., Boer, C., Schwarte, L.A., 2018. Correlation Coefficients: Appropriate Use and Interpretation. Anesth. Analg. 126, 1763–1768. https://doi.org/10.1213/ANE.0000000000002864.

Scroxton, N., Burns, S., Dawson, P., Rhodes, J.M., Brent, K., McGee, D., Heijnis, H., Gadd, P., Hantoro, W., Gagan, M., 2018. Rapid measurement of strontium in speleothems using core-scanning micro X-ray fluorescence. Chem. Geol. 487, 12–22. https://doi.org/10.1016/j.chemgeo.2018.04.008, 10.1016/j.chemgeo.2018.04.008.

Sharma, S., Bhattacharya, J.P., Richards, B., 2017. Source-to-sink sediment budget analysis of the Cretaceous Ferron Sandstone, Utah, U.S.A, using the fulcrum approach. J. Sediment. Res. 87, 594–608. https://doi.org/10.2110/jsr.2017.23.

Thomson, J., Croudace, I.W., Rothwell, R.G., 2006. A geochemical application of the ITRAX scanner to a sediment core containing eastern Mediterranean sapropel units. In: Geological Society Special Publication, vol. 267. Geological Society of London, pp. 65–77. https://doi.org/10.1144/GSL.SP.2006.267.01.05.

Tjallingii, R., Röhl, U., Kölling, M., Bickert, T., 2007. Influence of the water content on X-ray fluorescence corescanning measurements in soft marine sediments. G-cubed 8, 1–12. https://doi.org/10.1029/2006GC001393.

Tribovillard, N., Algeo, T.J., Lyons, T., Riboulleau, A., 2006. Trace metals as paleoredox and paleoproductivity proxies: An update. Chem. Geol. 232, 12–32. https://doi.org/10.1016/j.chemgeo.2006.02.012.

Turkistani, M.N., 2020. Micropaleontological (Foraminifera , Testate Amoeba) and μXRF Analysis of the Upper Cretaceous (Turonian) Notom Delta , Ferron Sandstone Member , Mancos Shale Formation , Centeral Utah , USA A Thesis Submitted to the School of Graduate Studies in the. Ph.D. thesis. McMaster University.

Turner, B.W., Tréanton, J.A., Slatt, R.M., 2016. The use of chemostratigraphy to refine ambiguous sequence stratigraphic correlations in marine mudrocks. An example from the Woodford Shale, Oklahoma, USA. J. Geol. Soc. 173, 854–868. https://doi.org/10.1144/jgs2015-125.

Wang, M.J., Zheng, H.B., Xie, X., Fan, D.D., Yang, S.Y., Zhao, Q.H., Wang, K., 2011. A 600-year flood history in the Yangtze River drainage: Comparison between a subaqueous delta and historical records. Chin. Sci. Bull. 56, 188–195. https://doi.org/10.1007/s11434-010-4212-2.

Ward, C.R., Kelloway, S.J., French, D., Wainwright, I.E., Marjo, C., Cohen, D.R., 2018. Profiling of inorganic elements in coal seams using laboratory-based core scanning X-ray fluorescence techniques. Int. J. Coal Geol. 191, 158–171. https://doi.org/10.1016/j.coal.2018.03.011, 10.1016/j.coal.2018.03.011.

Weltje, G.J., Bloemsma, M.R., Tjallingii, R., Heslop, D., Röhl, U., Croudace, I.W., 2015. Prediction of Geochemical Composition from XRF Core Scanner Data: A New Multivariate Approach Including Automatic Selection of Calibration Samples and Quantification of Uncertainties. In: Croudace, I.W., Rothwell, R.G. (Eds.), *Micro-XRF Studies of Sediment Cores: Applications of a Non-destructive Tool for the Environmental Sciences* Chapter 21. Springer Science+Business Media, pp. 507–534, 10.1007/978-94-017-9849-5. http://link.springer.com/10.1007/978-94-017-9849-5.

Weltje, G.J., Tjallingii, R., 2008. Calibration of XRF core scanners for quantitative geochemical logging of sediment cores: Theory and application. Earth Planet Sci. Lett. 274, 423–438. https://doi.org/10.1016/j.epsl.2008.07.054.

Wilson, R.D., Schieber, J., 2014. Muddy Prodeltaic Hyperpycnites in the Lower Genesee Group of Central New York, USA: Implications For Mud Transport In Epicontinental Seas. J. Sediment. Res. 84, 866–874, 10.2110/jsr.2014.70. http://jsedres.sepmonline.org/cgi/doi/10.2110/jsr.2014.70.

Wu, C., Bhattacharya, J.P., Ullah, M.S., 2015. Paleohydrology and 3D Facies Architecture of Ancient Point Bars, Ferron Sandstone, Notom Delta, South-Central Utah, U.S.A. J. Sediment. Res. 85, 399–418, 10.2110/jsr.2015.29. http://jsedres.sepmonline.org/cgi/doi/10.2110/jsr.2015.29.

Yoon, H., Ingraham, M.D., Grigg, J., Rosandick, B., Mozley, P., Rinehart, A., Mook, W.M., Dewers, T., 2019. Impact of Depositional and Diagenetic Heterogeneity on Multiscale Mechanical Behavior of Mancos Shale, New Mexico and Utah, USA. In: Camp, W., Milliken, K., Taylor, K., Fishman, N., Hackley, P., Macquaker, J. (Eds.), *Mudstone Diagenesis: Research Perspectives for Shale Hydrocarbon Reservoirs, Seals, and Source Rocks: AAPG Memoir 120* Chapter 8. American Association of Petroleum Geologists, pp. 121–148.

Zarriess, M., Johnstone, H., Prange, M., Steph, S., Groeneveld, J., Mulitza, S., MacKensen, A., 2011. Bipolar seesaw in the northeastern tropical Atlantic during Heinrich stadials. Geophys. Res. Lett. 38, 3–8. https://doi.org/10.1029/2010GL046070.

Zarriess, M., Mackensen, A., 2010. The tropical rainbelt and productivity changes off northwest Africa: A 31,000-year high-resolution record. Mar. Micropaleontol. 76, 76–91. https://doi.org/10.1016/j.marmicro.2010.06.001, 10.1016/j.marmicro.2010.06.001.

Zhu, Y., Bhattacharya, J.P., Li, W., Lapen, T.J., Jicha, B.R., Singer, B.S., 2012. Milankovitch-Scale Sequence Stratigraphy and Stepped Forced Regressions of the Turonian Ferron Notom Deltaic Complex, South-Central Utah, U.S.A. J. Sediment. Res. 82, 723–746, 10.2110/jsr.2012.63. http://jsedres.sepmonline.org/cgi/doi/10.2110/jsr.2012.63.